

# HESSIAN-INVERSION-FREE RAY-BORN INVERSION FOR HIGH-RESOLUTION QUANTITATIVE ULTRASOUND TOMOGRAPHY

ASHKAN JAVAHERIAN

*Department of Medical Physics & Biomedical Engineering,  
University College London, London, UK. WC1E 6BT*

## ABSTRACT

This study proposes a Hessian-inversion-free ray-born inversion approach for biomedical ultrasound tomography. The proposed approach is a more efficient version of the ray-born inversion approach proposed in [1]. Using these approaches, the propagation of acoustic waves are modelled using a ray approximation to heterogeneous Green's function. The inverse problem is solved in the frequency domain by iteratively linearisation and minimisation of the objective function from low to high frequencies. In [1], the linear subproblem associated with each frequency interval is solved by an implicit and iterative inversion of the Hessian matrix (inner iterations). Instead, this study applies a preconditioning approach to each linear subproblem so that the Hessian matrix becomes diagonalised, and can thus be inverted in a single step. Using the proposed preconditioning approach, the computational cost of solving each linear subproblem of the proposed ray-Born inversion approach becomes almost the same as solving one linear subproblem associated with a radon-type time-of-flight-based approach using bent rays. More importantly, the smoothness assumptions made for diagonalising the Hessian matrix make the image reconstruction more stable than the inversion approach in [1] to noise.

## 1. INTRODUCTION

The aim of ultrasound tomography (UST) is to determine the map of acoustic properties of interior of an object from ultrasonic measurements made on its boundary. Ultrasound tomography has received growing interest for medical diagnosis [2, 3] and industrial monitoring [4, 5]. One of the most important application of UST for medical diagnosis is detection of malignant tumours in the breast [2, 6, 7, 8, 9].

Ideally, the information which can be determined from ultrasound data measured on the boundary of an object include quantitative distribution of the sound speed, absorption and density, and a qualitative map of gradient of acoustic impedance [3]. This manuscript is concentrated on the reconstruction of the sound speed, so the term UST is used for the sound speed reconstruction. Approaches to image reconstruction of the sound speed from UST data can be categorised by: 1) the data type used in the inversion, 2) whether the objective function to be minimised is nonlinear or linearised, 3) whether the objective function is defined in the time domain or frequency domain, or 4) the forward model used.

---

*E-mail address:* a.javaherian@ucl.ac.uk.

*Date:* October 2022.

In terms of the data type used, the first class of approaches use only the direct times-of-flight between the emitters and receivers [10], and no scattered waves are included. The second uses the complete measured time series, including the scattered waves [11, 12, 13, 14, 15, 16, 17, 18, 19, 20]. The third uses the direct-arrival and first-scattered waves [21, 22, 23, 24, 25, 26, 27, 28, 29, 30, 31]. In our study, the first and third data types are used, the former for providing an initial guess and the latter for solving the main inverse problem. The approach we use for solving the main inverse problem is based on an iterative linearisation of the objective function, and performs the linearisations in the frequency domain from low to high frequencies. The forward problem is modelled based on a ray-approximation to the heterogeneous Green’s function. The motivation for our chosen forward model is that ray theory based on high frequency approximation provides a good trade-off between accuracy and computational cost when data is broadband [33]. In addition, the known limitation of ray theory such as caustic or multivaluedness of the minimal acoustic length [34] is less challenging for imaging soft tissues like the breast with refractive index often varying between 0.9 – 1.1 than seismic imaging applications with sharp changes in the refractive index. The details of our UST inversion approach are given in [1]. It was numerically shown that this approach can reconstruct a high resolution map of the sound speed, but it is computationally few orders of magnitude less costly than full-wave inversion approaches using full solution of the wave equation [16, 17, 18, 19, 20].

The common approaches accounting for diffraction or singly scattered waves use the Green’s function in the homogeneous medium, and only account for the acoustic heterogeneity in the scattering potential [21, 22, 23, 24, 25, 26, 27, 28, 29, 30, 31], but it was shown that combining ray theory with the Born inversion can significantly improve the accuracy via including the sound speed heterogeneity, refraction and acoustic absorption and dispersion in the Green’s functions predicting the incident and scattered waves [1]. In [32], a one-step inversion approach combining the diffraction tomography with ray tracing on an ad-hoc basis was proposed, in which aberration of phase of the Green’s function due to heterogeneities was accounted for by performing ray tracing on an image reconstructed using a time-of-flight-based approach, but the procedure taken for the inversion does not follow the common optimisation approaches.

The UST inversion approach recently proposed in [1] can be fit into a class of linearised inversion approaches, known as ray-born migration/inversion, in the context of inverse seismic theory [35, 36, 33, 37]. In [1], the objective function is discretised in the frequency domain, and is linearised and minimised over the frequency range covered by the ultrasound transducers. This is done by dividing the frequency range into a number of frequency intervals, each including a fixed number, here 2, of the discretised frequencies, and performing the minimisation sequentially from low to high frequency intervals such that the solution of the linearised subproblem for each frequency interval is used as initial guess for the linearised subproblem associated with the next frequency interval. Because the inverse problem of reconstructing acoustic parameters from ultrasound or seismic data is nonlinear, minimising the objective function from low to high frequencies helps avoiding getting stuck in the local minima [13, 15, 38].

In [1], each linearised subproblem, which is equivalent to the product of the inverse of the Hessian matrix by the gradient of the objective function, is solved implicitly using a Conjugate Gradient (CG) algorithm via an iterative implementation of the Fréchet derivative of the forward operator and its adjoint. Because of the iterative computation of the Hessian matrix, the computational cost for solving each linearised subproblem using this approach is less than an order of magnitude more than solving a linearised subproblem associated with a radon-type time-of-flight-based approach, whose major computational cost corresponds to only two-point ray tracing. (Using the CPU mentioned in section 6.1, the total computational time for image reconstruction using the inversion

approach in [1] is almost the same as numerically solving a single forward problem of the full-Wave inversion using an efficient numerical approach for simulating the propagation of acoustic waves [39, 40].) For further reducing the computational cost, this study proposes a noniterative approach for solving the linearised subproblem associated with each frequency set. The proposed approach is based on preconditioning the arising linearised subproblems such that the Hessian matrix becomes diagonalised and can thus be directly inverted. Using the proposed approach, the computational cost of each iteration (linearised subproblem) of the ray-born minimisation approach is reduced to almost that of the radon-type time-of-flight-based inversion approaches using bent rays [41].

Section 2 introduces the forward and inverse problems of UST based on a Green's function solution to the frequency-domain Helmholtz wave equation for heterogeneous and absorbing media. In section 3, the proposed approach for solving the inverse problem based on the heterogeneous Green's function is explained. Section 4 describes ray tracing and how the Green's function for heterogeneous media is approximated based on the ray theory. Section 5 explains the procedure for discretising the forward and inverse problems. In section 6, the ray approximation to heterogeneous Green's function is numerically validated, and the reconstructed images demonstrating the performance of the proposed Hessian-inversion-free ray-born inversion approach are presented, and compared to the inversion approach in [1].

## 2. GREEN'S FUNCTION SOLUTION TO THE WAVE EQUATION

This section describes the forward and inverse problems of image reconstruction of the sound speed. Let  $\mathbf{x} = (x^1, \dots, x^d)$  denote a spatial position in  $\mathbb{R}^d$  with  $d$  the number of dimensions. In general,  $d$  can be either 2 or 3. This study is restricted to  $d = 2$ , but an extension to  $d = 3$  is straightforward. Accordingly,  $\Omega \subset \mathbb{R}^d$  is an open bounded set, and contains the spatially-varying part of the sound speed distribution,  $c(\mathbf{x})$ , i.e.,  $(c(\mathbf{x})/c_0 - 1) \in c_0^\infty$ , where  $c_0$  is a scalar value representing the sound speed outside  $\Omega$  (here the sound speed in water). The open set  $\Omega$  is bounded by a circular ring  $\mathbb{S} \subset \mathbb{R}$  containing the emission and reception points  $e$  and  $r$ . (Without loss of generality, the emission and reception elements are assumed points.) Each emission element, referred to here as emitter  $e \in \{1, \dots, N_e\}$ , is sequentially excited by a pulse and acts as a source  $s(t; \mathbf{x}_e)$  within the excitation time  $t \in (0, T_s)$ . The acoustic pressure field produced by each emitter propagates across the object in water and is measured at the reception elements, referred to here as receiver  $r \in \{1, \dots, N_r\}$ , for times  $t \in (0, T)$  with  $T \gg T_s$ . For each excitation element  $e$ , centred at  $\mathbf{x}_e$ , the time series measured by the receiver  $r$ , centered at  $\mathbf{x}_r$ , is represented by  $p(t, \mathbf{x}_r; \mathbf{x}_e)$ . The inverse problem is an image reconstruction of  $c(\mathbf{x})$  from the measured boundary pressure times series  $p(t, \mathbf{x}_r; \mathbf{x}_e)$  for all emitter-receiver pairs.

While the data is typically measured in the time domain, i.e. with a broadband excitation signal, the image reconstruction is here performed in the frequency domain. To this end, we define the following Fourier transform pair between the time and temporal frequency domains,

$$p(\omega) = \mathcal{F}p(t) = \int_{-\infty}^{\infty} p(t)e^{i\omega t} dt, \quad p(t) = \mathcal{F}^{-1}p(\omega) = \frac{1}{2\pi} \int_{-\infty}^{\infty} p(\omega)e^{-i\omega t} dt. \quad (1)$$

**2.1. Lossy Helmholtz equation and complex wavevector.** The propagation of single frequency acoustic pressure field,  $p(\omega, \mathbf{x})$ , in an absorbing medium is often modelled using a lossy Helmholtz equation of the form

$$\left(\tilde{k}(\mathbf{x})^2 + \nabla^2\right)p(\omega, \mathbf{x}; \mathbf{x}_e) = -s(\omega, \mathbf{x}_e), \quad \tilde{k} = |\tilde{\mathbf{k}}|, \quad (2)$$

where  $\tilde{\mathbf{k}}$  is a complex wavevector  $\tilde{\mathbf{k}} = \mathbf{k} + i\mathbf{k}_i$ , where the real part  $\mathbf{k}$  is related to the phase speed  $c_p(\omega)$  of the wave by

$$|\mathbf{k}| \equiv k = \omega/c_p(\omega), \quad (3)$$

and the imaginary part is related to the absorption coefficient  $\alpha$  by

$$\mathbf{k}_i = \alpha(\mathbf{k}/k). \quad (4)$$

The specific form of the wavenumber we use is in the form [42]

$$\tilde{k} = k + i\alpha = \frac{\omega}{c} + \alpha(\tan(\pi y/2) + i), \quad (5)$$

where the absorption follows the frequency power law  $\alpha = \alpha_0\omega^y$ . Here,  $\alpha_0$  has units  $\text{Np}(\text{rad/s})^{-y}\text{m}^{-1}$ , and  $y$  is the power-law exponent with a non-integer often in the range  $1 \leq y \leq 1.5$  for soft tissue [43, 44]. The solution of (2) in terms of Green's function can be written as

$$p(\omega, \mathbf{x}) = \int g(\omega, \mathbf{x}; \mathbf{x}') s(\omega, \mathbf{x}') d\mathbf{x}', \quad (6)$$

where  $g(\omega, \mathbf{x}; \mathbf{x}')$  is the Green's function at point  $\mathbf{x}$ , originated from point  $\mathbf{x}'$ , associated with frequency  $\omega$ , and satisfies

$$\left(\tilde{k}(\mathbf{x})^2 + \nabla^2\right) g(\omega, \mathbf{x}; \mathbf{x}') = -\delta(\mathbf{x} - \mathbf{x}'). \quad (7)$$

For the 2D case, the Green's function for the heterogeneous and absorbing media can be written in the form

$$g(\omega, \mathbf{x}; \mathbf{x}') \approx A(\mathbf{x}; \mathbf{x}') \exp(i(\phi(\mathbf{x}; \mathbf{x}') + \pi/4)). \quad (8)$$

Here,  $\phi$  is the phase, and  $A = A_{abs}A_{geom}$  is the amplitude factor, and contains contributions from absorption as well as geometric spreading. All these parameters are approximated using the ray theory [34].

### 3. MINIMISATION APPROACH

This section explains the approach taken for minimising the objective function. The objective function in terms of Green's function in the frequency domain is defined in the form

$$\mathcal{F}(c) = \frac{1}{2} \sum_{e,r} \int \delta g_{res}^* \mathcal{Q} \delta g_{res} d\omega, \quad (9)$$

where  $\mathcal{Q}$  is a covariance matrix, and  $\delta g_{res}$  is the *residual*, and has components

$$\delta g_{res}(c; \omega, r; e) = g_{(c;\omega;\mathbf{x}_r;\mathbf{x}_e)} - \hat{g}_{(\omega,r;e)}. \quad (10)$$

Here,  $\hat{g}_{(\omega,r;e)}$  is the *measured Greens function* at point  $\mathbf{x}_r$ , originated from point  $\mathbf{x}_e$ , and associated with frequency  $\omega$ , and can be obtained by deconvolution of the measured pressure  $\hat{p}_{(\omega,r;e)}$  from the excitation pulse  $s(\omega; \mathbf{x}_e)$  in the frequency domain.

A linearisation of the objective function (9) associated with the frequency interval  $\omega$  around the sound speed update  $c^{(n)}$  yields

$$\delta c^{(n)} \approx \arg \min_{\delta c} \frac{1}{2} \sum_{e,r} \int \mathcal{Q} |\delta g_{(c^{(n)};\omega;\mathbf{x}_r;\mathbf{x}_e)}(\delta c) - \delta g_{res}(c^{(n)};\omega, r; e)|^2 d\omega, \quad (11)$$

which seeks to find the search direction  $\delta c^{(n)}$  which fits the induced perturbed Green's function on the receivers, i.e.,

$$\delta g_{(c^{(n)}; \omega, \mathbf{x}_r; \mathbf{x}_e)}(\delta c) = \frac{\partial g_{(c^{(n)}; \omega, \mathbf{x}_r; \mathbf{x}_e)}}{\partial c^{(n)}(\mathbf{x})} \delta c \quad (12)$$

to the residual in a least square sense. The minimisation of (11) is equivalent to solving the linear equation

$$\nabla \mathcal{F}^{(n)}(\mathbf{x}) + \int H^{(n)}(\mathbf{x}; \mathbf{x}') \delta c^{(n)}(\mathbf{x}') d\mathbf{x}' = 0, \quad (13)$$

where the first term on the left-hand side is the gradient of  $\mathcal{F}$  at iteration  $n$ , and the second term is the action of the Hessian,  $H^{(n)}$ , on a perturbation  $\delta c^{(n)}$ . The gradient  $\nabla \mathcal{F}^{(n)}$  can be written as

$$\begin{aligned} \nabla \mathcal{F}^{(n)}(\mathbf{x}) &= \sum_{e,r} \int \left( \frac{\partial g_{(c^{(n)}; \mathbf{x}_r; \mathbf{x}_e)}}{\partial c^{(n)}(\mathbf{x})} \right)^* \mathcal{Q} \delta g_{res}(c^{(n)}; r; e) d\omega, \\ &= \sum_{e,r} \int \left( g(c^{(n)}; \mathbf{x}_r; \mathbf{x}) \Upsilon(c^{(n)}; \mathbf{x}) g(c^{(n)}; \mathbf{x}; \mathbf{x}_e) \right)^* \mathcal{Q} \delta g_{res}(c^{(n)}; r; e) d\omega, \end{aligned} \quad (14)$$

where  $*$  stands for the conjugate transpose, and  $\omega$  has been dropped for brevity. Also,

$$\Upsilon(c^{(n)}; \omega, \mathbf{x}) = \frac{-2\omega}{c^{(n)}(\mathbf{x})^2} k^{(n)}(\mathbf{x}), \quad (15)$$

where  $k^{(n)}$  satisfies (5) for  $c^{(n)}$  and  $\alpha$ . (We have used the assumption that  $\alpha$  is known, and is thus not changed with  $n$ ). Also, the action  $H^{(n)}(\mathbf{x}; \mathbf{x}') \delta c^{(n)}(\mathbf{x}')$  yields [1]

$$\begin{aligned} &\sum_{e,r} \int \left( \frac{\partial g_{(c^{(n)}; \mathbf{x}_r; \mathbf{x}_e)}}{\partial c^{(n)}(\mathbf{x})} \right)^* \mathcal{Q} \delta g_{(c^{(n)}; \mathbf{x}_r; \mathbf{x}_e)} d\omega \\ &= \sum_{e,r} \int \left( g(c^{(n)}; \mathbf{x}_r; \mathbf{x}) \Upsilon(c^{(n)}; \mathbf{x}) g(c^{(n)}; \mathbf{x}; \mathbf{x}_e) \right)^* \mathcal{Q} \\ &\quad \left( g(c^{(n)}; \mathbf{x}_r; \mathbf{x}') \Upsilon(c^{(n)}; \mathbf{x}') \delta c^{(n)}(\mathbf{x}') g(c^{(n)}; \mathbf{x}'; \mathbf{x}_e) \right) d\omega, \end{aligned} \quad (16)$$

where,  $\Upsilon(c^{(n)}; \mathbf{x}) \delta c^{(n)}(\mathbf{x})$  is the scattering potential at point  $\mathbf{x}$ . By plugging (8) into the above equation, the Hessian matrix is recast in the form

$$H^{(n)}(\mathbf{x}; \mathbf{x}') = \sum_{e,r} \int \mathcal{Q} \mathcal{D}(c^{(n)}; \omega, \mathbf{x}; \mathbf{x}'; r; e) e^{-i\Phi(c^{(n)}; \omega, \mathbf{x}; \mathbf{x}'; r; e)} d\omega, \quad (17)$$

where

$$\begin{aligned} \mathcal{D}(c^{(n)}; \omega, \mathbf{x}; \mathbf{x}'; \mathbf{x}_r; \mathbf{x}_e) &= \left( A(c^{(n)}; \omega, \mathbf{x}_r; \mathbf{x}) \Upsilon(c^{(n)}; \omega, \mathbf{x}) A(c^{(n)}; \omega, \mathbf{x}; \mathbf{x}_e) \right)^* \\ &\quad \left( A(c^{(n)}; \omega, \mathbf{x}_r; \mathbf{x}') \Upsilon(c^{(n)}; \omega, \mathbf{x}') A(c^{(n)}; \omega, \mathbf{x}'; \mathbf{x}_e) \right), \end{aligned} \quad (18)$$

and

$$\begin{aligned} \Phi(c^{(n)}; \omega, \mathbf{x}; \mathbf{x}'; \mathbf{x}_r; \mathbf{x}_e) &= \phi(c^{(n)}; \omega, \mathbf{x}_r; \mathbf{x}) + \phi(c^{(n)}; \omega, \mathbf{x}; \mathbf{x}_e) \\ &\quad - \left( \phi(c^{(n)}; \omega, \mathbf{x}_r; \mathbf{x}') + \phi(c^{(n)}; \omega, \mathbf{x}'; \mathbf{x}_e) \right). \end{aligned} \quad (19)$$

Now, the following two approximations are enforced on (17) [33, 35, 36, 37].

$$\mathcal{D}(c^{(n)}; \omega, \mathbf{x}; \mathbf{x}'; \mathbf{x}_r; \mathbf{x}_e) \approx \mathcal{D}(c^{(n)}; \omega, \mathbf{x}'; \mathbf{x}'; \mathbf{x}_r; \mathbf{x}_e) \quad (20)$$

and

$$\begin{aligned} \Phi(c^{(n)}; \omega, \mathbf{x}; \mathbf{x}'; \mathbf{x}_r; \mathbf{x}_e) &\approx \nabla_{\mathbf{x}'} \left( \phi(c^{(n)}; \omega, \mathbf{x}_r; \mathbf{x}') + \phi(c^{(n)}; \omega, \mathbf{x}'; \mathbf{x}_e) \right) \cdot (\mathbf{x} - \mathbf{x}') \\ &= \mathbf{k}(c^{(n)}; \omega, \mathbf{x}'; \mathbf{x}_r; \mathbf{x}_e) \cdot (\mathbf{x} - \mathbf{x}'). \end{aligned} \quad (21)$$

Here,  $\mathbf{k}(\mathbf{x}; \mathbf{x}_r; \mathbf{x}_e)$  is the gradient of the two-way isochron, the curve in the 2D space of the scattering point  $\mathbf{x}$  on which the sum of accumulated phase from the source  $e$  to the scatterer  $\mathbf{x}$  and from scatterer  $\mathbf{x}$  to the receiver  $r$  is equal [35, 36].  $\mathbf{k}(\mathbf{x}; \mathbf{x}_r; \mathbf{x}_e)$  is thus a vector passing through  $\mathbf{x}$ , normal to the two-way isochron, and satisfies  $\mathbf{k}(\mathbf{x}; \mathbf{x}_r; \mathbf{x}_e) = \omega \mathbf{p}(\mathbf{x}; \mathbf{x}_r; \mathbf{x}_e)$ , where  $\mathbf{p}(\mathbf{x}; \mathbf{x}_r; \mathbf{x}_e) = \mathbf{p}(\mathbf{x}, \mathbf{x}_e) + \mathbf{p}(\mathbf{x}_r, \mathbf{x}) = \mathbf{p}(\mathbf{x}, \mathbf{x}_e) - \mathbf{p}(\mathbf{x}, \mathbf{x}_r)$  with  $\mathbf{p}(\mathbf{x}, \mathbf{x}_e)$  (resp.  $\mathbf{p}(\mathbf{x}, \mathbf{x}_r)$ ) the slowness vector of the ray initialised at  $e$  (resp.  $r$ ) at point  $\mathbf{x}$ .

Note that for sufficiently distant  $\mathbf{x}$  and  $\mathbf{x}'$ ,  $\Phi(c^{(n)}; \omega, \mathbf{x}; \mathbf{x}'; \mathbf{x}_r; \mathbf{x}_e)$  becomes large, and therefore,  $H(\mathbf{x}; \mathbf{x}')$  in (17) becomes negligible. Therefore, the assumption (20) implies that  $A(\mathbf{x}) \approx A(\mathbf{x}')$  and  $\Upsilon(\mathbf{x}) \approx \Upsilon(\mathbf{x}')$ , when  $\mathbf{x}$  and  $\mathbf{x}'$  are close sufficiently that  $H(\mathbf{x}; \mathbf{x}')$  becomes large. In addition, (21) implies that  $\Phi(c^{(n)}; \omega, \mathbf{x}; \mathbf{x}'; \mathbf{x}_r; \mathbf{x}_e)$  changes linearly with  $\mathbf{x} - \mathbf{x}'$  for sufficiently close  $\mathbf{x}$  and  $\mathbf{x}'$ . These two assumptions together apply some smoothness on the reconstructed image, compared to the approach used in [1], which is based on the iterative inversion of the full Hessian matrix.

Now, by plugging the approximations (20) and (21) into (17), the Hessian matrix is reduced to the form

$$H^{(n)}(\mathbf{x}; \mathbf{x}') = \sum_{e,r} \int \mathcal{Q} \mathcal{D}(c^{(n)}; \omega, \mathbf{x}'; \mathbf{x}'; r; e) e^{-i\mathbf{k}(c^{(n)}; \omega, \mathbf{x}'; \mathbf{x}_r; \mathbf{x}_e) \cdot (\mathbf{x} - \mathbf{x}')} d\omega. \quad (22)$$

Now, by assuming that rays do not have caustics or any other singularities, a one-to-one map  $(e, r) \rightarrow (\theta, \zeta)$  is defined. (These assumptions hold, because the range of the changes in the sound speed in soft tissues like the breast is less than 15%.) Here, on each arbitrary point  $\mathbf{x} \in \Omega$ , and emitter-receiver pair  $(e, r)$ ,  $\theta$  is defined as the scattering angle, which satisfies

$$\theta(\mathbf{x}; \mathbf{x}_r; \mathbf{x}_e) = \gamma_e(\mathbf{x}) - (\gamma_r(\mathbf{x}) - \pi), \quad (23)$$

where  $\gamma_e(\mathbf{x})$  and  $\gamma_r(\mathbf{x})$  are the angle components (in the polar coordinates) of the slowness vector of rays initialised from emitter  $e$  and receiver  $r$  at point  $\mathbf{x}$ , respectively. Also,  $\zeta$  is defined as the angle of the two-way wavevector  $\mathbf{k}(\mathbf{x}; \mathbf{x}_r; \mathbf{x}_e)$ , which is normal to the two-way isochron at point  $\mathbf{x}$  with respect to emitter-receiver pair  $(e, r)$ , and satisfies

$$\zeta(\mathbf{x}; \mathbf{x}_r; \mathbf{x}_e) = \frac{1}{2}(\gamma_e(\mathbf{x}) + \gamma_r(\mathbf{x}) - \pi). \quad (24)$$

Also, the magnitude of the two-way wavevector satisfies

$$|\mathbf{k}| = 2 \frac{\omega}{c} \cos\left(\frac{\theta}{2}\right). \quad (25)$$

Applying the one-to-one map  $(e, r) \rightarrow (\theta, \zeta)$  and a change of variable of the integration from  $\omega$  to  $|\mathbf{k}|$  on (22) gives

$$H^{(n)}(\mathbf{x}; \mathbf{x}') = \sum_{\theta} \sum_{\zeta} \int \frac{\mathcal{Q} \mathcal{D}(c^{(n)}; \omega, \mathbf{x}'; \mathbf{x}'; r; e)}{|\mathbf{p}(c^{(n)}; \omega, \mathbf{x}'; \mathbf{x}_r; \mathbf{x}_e)|} e^{-i\mathbf{k}(c^{(n)}; \omega, \mathbf{x}'; \mathbf{x}_r; \mathbf{x}_e) \cdot (\mathbf{x} - \mathbf{x}')} d|\mathbf{k}|, \quad (26)$$

and the fact that  $\left| \frac{d\omega}{d|\mathbf{k}|} \right| = 1/|\mathbf{p}|$ , where  $|\mathbf{p}| = 2/c \cos(\theta/2)$ . Following [33, 35, 36, 37], we now choose  $\mathcal{Q}$  such that  $H^{(n)}(\mathbf{x}; \mathbf{x}')$  be diagonalised and can thus be directly inverted. Accordingly, by choosing

$$\mathcal{Q}(c^{(n)}; \omega, \mathbf{x}'; \mathbf{x}_r; \mathbf{x}_e) = \frac{\omega}{(2\pi)^2} \frac{|\mathbf{p}(c^{(n)}; \omega, \mathbf{x}'; \mathbf{x}_r; \mathbf{x}_e)|^2}{\mathcal{D}(c^{(n)}; \omega, \mathbf{x}'; \mathbf{x}_r; \mathbf{x}_e)}, \quad (27)$$

the Hessian matrix in (22) collapses to

$$H^{(n)}(\mathbf{x}, \mathbf{x}') = \sum_{\theta} \left( \frac{1}{(2\pi)^2} \sum_{\zeta} \int |\mathbf{k}| e^{-i\mathbf{k}(\mathbf{x}') \cdot (\mathbf{x} - \mathbf{x}')} d|\mathbf{k}| \right) \approx \sum_{\theta} \delta(\mathbf{x} - \mathbf{x}') = a\delta(\mathbf{x} - \mathbf{x}'), \quad (28)$$

where  $a$  is a scalar with  $\lim_{(\Delta e, \Delta r) \rightarrow 0} a = 2\pi$  with  $\Delta e$  and  $\Delta r$  representing the fixed arc spacing of the emitters and receivers, respectively. We have also used the fact that the term inside the parenthesis in (28) can be expressed as a discretised and band-limited version of the exact Fourier transform of the delta function in the cylindrical coordinates [35], i.e.,

$$\frac{1}{(2\pi)^2} \int_{\zeta=0}^{2\pi} \int_{-\infty}^{+\infty} |\mathbf{k}| e^{-i\mathbf{k}(\mathbf{x}') \cdot (\mathbf{x} - \mathbf{x}')} d|\mathbf{k}| d\zeta = \delta(\mathbf{x} - \mathbf{x}'). \quad (29)$$

Now, plugging the preconditioning matrix in (27) into the functional gradient (14), and then plugging (14) into the linearised equation (13), give a search direction

$$\delta c^{(n)}(\mathbf{x}) = \sum_{e, r, \omega} \Lambda(c^{(n)}; \omega; \mathbf{x}; \mathbf{x}_r; \mathbf{x}_e) \delta g_{res}(c^{(n)}; \omega, r; e), \quad (30)$$

where we have also used (28). Here,

$$\Lambda(c^{(n)}; \omega, \mathbf{x}; \mathbf{x}_r; \mathbf{x}_e) = \frac{\omega \Delta\omega}{(2\pi)^3} \left( \frac{|\mathbf{p}(c^{(n)}; \omega, \mathbf{x}; \mathbf{x}_r; \mathbf{x}_e)|^2}{\Upsilon(c^{(n)}; \omega; \mathbf{x})} g^{\dagger}(c^{(n)}; \omega, \mathbf{x}; \mathbf{x}_e) \right) g^{\dagger}(c^{(n)}; \omega, \mathbf{x}; \mathbf{x}_r), \quad (31)$$

where

$$g^{\dagger}(c^{(n)}; \omega, \mathbf{x}; \mathbf{x}') = \frac{e^{-i\phi(c^{(n)}; \omega, \mathbf{x}; \mathbf{x}')}}{A(c^{(n)}; \omega; \mathbf{x}; \mathbf{x}')} \quad (32)$$

Here,  $g^{\dagger}$  is called inverse Green's function, where  $\dagger$  indicates that the Green's function is reversed in both phase and amplitude. Note also that in  $g^{\dagger}(c^{(n)}; \omega, \mathbf{x}; \mathbf{x}_r)$ , which acts on  $\delta g_{res}(c^{(n)}; r; e)$ , the reciprocity of Green's function has been used [46]. In addition, after discretisation, the Hessian matrix and gradient are, respectively, multiplied by  $(\Delta\mathbf{x})^2$  and  $\Delta\mathbf{x}$  to account for spatial sampling, where  $\Delta\mathbf{x}$  stands for the area of each pixel. Therefore, a spatially discretised version of (30) gives updates  $c^{(n+1)}(\mathbf{x}) = c^{(n)}(\mathbf{x}) + \tau (\Delta\mathbf{x})^{-1} \delta c^{(n)}(\mathbf{x})$ , where  $\tau$  is the step length.

#### 4. RAY TRACING

This section describes a numerical implementation of the method described above for implementing UST. Specifically, this section explains how the ray theory based on a high frequency approximation is used for computing the terms in the approximate Green's function and its inverse variant for heterogeneous and absorbing media.

In general, rays are curves that are perpendicular to surfaces of constant phase, i.e., they are tangent to the wavevector  $\mathbf{k}$ , which satisfies

$$\mathbf{k} = \nabla\phi, \quad (33)$$

and therefore the eikonal equation

$$\nabla\phi \cdot \nabla\phi = k^2. \quad (34)$$

The eikonal equation can be expressed in the form of a Hamiltonian

$$H(\mathbf{x}, \mathbf{k}) = \frac{1}{2} (\mathbf{k} \cdot \mathbf{k} - k^2), \quad (35)$$

where we remind that  $k$  is the real part of  $\tilde{k}$ , which is dependent on  $c$  through Eq. (5). The Hamiltonian yields  $H = 0$  along a reference ray satisfying the canonical equations

$$\begin{aligned} \dot{\mathbf{x}} &= \nabla_{\mathbf{k}} H \\ \dot{\mathbf{k}} &= -\nabla_{\mathbf{x}} H. \end{aligned} \quad (36)$$

We introduce the canonical vector of the reference ray as  $\mathbf{y}_0(s) = (\mathbf{x}_0(s), \mathbf{k}_0(s))^T$ , where  $s$  is the arc length along the ray, and  $T$  is the transpose operator. The contributions of the amplitude factor  $A$  in Eq. (8) from the geometrical spreading is  $A_{geom}$ , and is determined by how the area of the ray tube changes compared to a reference point on the ray, and relies on the concept of the ray Jacobian [34]. In [1], the ray Jacobian was defined by the rate at which two closely-spaced rays diverge, and was computed using finite differences. (cf. [34], section 3.10.4.3.) Computing the ray Jacobian using finite differences requires at least two additional auxiliary rays in 2D (or three auxiliary rays in 3D). Here, the ray Jacobian is computed using *paraxial* ray tracing, also known as *dynamic* ray tracing. Instead of tracing auxiliary rays independent from the reference ray, paraxial ray tracing involves solving an additional system of linear ordinary differential equations for tracing paraxial ray, which can be solved simultaneously with the ray tracing system for the reference ray. (cf. [34], section 3.10.4.4.) Note that the paraxial rays are traced only along the optimal rays, which link the emitter-receiver pairs.

Accordingly, a paraxial ray is defined by  $\mathbf{y}(s) = (\mathbf{x}(s), \mathbf{k}(s))^T$ . Here,  $\mathbf{y}(s) = \mathbf{y}_0(s) + \delta\mathbf{y}(s)$ , where  $\delta\mathbf{y}(s) = (\delta\mathbf{x}(s), \delta\mathbf{k}(s))^T$  is the perturbation to the canonical vector of the reference ray, and satisfies the paraxial ray tracing system of equations

$$\delta\dot{\mathbf{y}} = \mathbf{D} \delta\mathbf{y}, \quad (37)$$

where

$$\mathbf{D} = \begin{bmatrix} \nabla_{\mathbf{x}} \nabla_{\mathbf{k}} H & \nabla_{\mathbf{k}} \nabla_{\mathbf{k}} H \\ -\nabla_{\mathbf{x}} \nabla_{\mathbf{x}} H & -\nabla_{\mathbf{k}} \nabla_{\mathbf{x}} H \end{bmatrix}. \quad (38)$$

Using the ray equations (36), the unit vector  $d\mathbf{x}/ds$  and the wavevector  $\mathbf{k}$  satisfy the ray equations

$$\frac{d\mathbf{x}}{ds} = \frac{\mathbf{k}}{k}, \quad \frac{d\mathbf{k}}{ds} = \nabla k. \quad (39)$$

Also, using (37) and (38), the paraxial ray equations are in the form

$$\frac{d}{ds} \delta\mathbf{x} = \frac{\delta\mathbf{k}}{k}, \quad \frac{d}{ds} \delta\mathbf{k} = \left( \frac{1}{k^2} \nabla k \nabla k^T + \frac{1}{k} \nabla^2 k \right) \delta\mathbf{x}. \quad (40)$$

Note that in (39) and (40), a change of variable has been performed in space for ensuring the unitarity of the direction vector  $d\mathbf{x}/ds$ . Here, the paraxial ray tracing system defined by (39) and (40) is numerically implemented using a second-order variant of Runge-Kutta (RK) scheme, known as Heun's method, which provides a good compromise between accuracy and speed [47, 48]. An outline of the Heun's approach for solving the paraxial ray tracing system is given in Algorithm 1. The system (38) is a ray, if the perturbation vector  $\delta\mathbf{y}$  satisfies

$$\delta H = \nabla_{\mathbf{k}} H \cdot \delta\mathbf{k} + \nabla_{\mathbf{x}} H \cdot \delta\mathbf{x} = 0. \quad (41)$$

In addition, considering (39),  $\delta H$  is constant along any solutions of the paraxial system, so it is sufficient to ensure the condition (41) at the initial point [49].

*Initial conditions:* The initial wavevector is specified by the frequency  $\omega$ , the sound speed in water  $c_0$  and the initial unit vector. Following [1], the rays are initialised from  $\mathbf{x}_e$  and are connected to  $\mathbf{x}_r$  through ray linking [41]. The parameters of the Green's function on point  $\mathbf{x}$  is then computed by interpolation from the linked rays onto the point  $\mathbf{x}$ . Ray-linking is in class of shooting methods, and seeks to find a ray trajectory which provides the stationary path within a family of neighborhood paths between  $\mathbf{x}_e$  and  $\mathbf{x}_r$  by enforcing a boundary condition on the rays' path such that the ray initialised from an emitter  $e$  is intercepted by the receiver  $r$  after travelling across the medium. For each iteration (linear subproblem) of the UST inverse problem, and emitter–receiver pair  $(e, r)$ , ray linking is performed by iteratively determining the initial angle of the ray initialised from the emitter  $e$  using an optimisation algorithm such that the interception point of the ray by the detection surface (ring) matches the position of the receiver  $r$  within a tolerance [34, 50]. Having determined the initial wavevector  $\mathbf{k}(s_0)$  and using the condition (41), together with enforcing the constraint  $\delta\mathbf{x}(s_0) = 0$ , the initial perturbation to the wavevector  $\delta\mathbf{k}(s_0)$  must satisfy  $\mathbf{k}(s_0) \cdot \delta\mathbf{k}(s_0) = 0$ .

---

**Algorithm 1** Paraxial ray tracing for the forward field using Heun's method
 

---

```

1: input:  $\mathbf{x}_e, k := k(\mathbf{x})$                                 ▷ Input initial ray position and wavenumber
2: initialise:  $\mathbf{x}, \mathbf{k}$                                     ▷ Set initial conditions: reference ray
3:  $\delta\mathbf{x} = 0, \delta\mathbf{k}$  satisfying  $\delta\mathbf{k} \cdot \mathbf{k} = 0$ ,          ▷ Set initial conditions: paraxial ray (amplitude)
4: while  $\mathbf{x}(s)$  is inside  $\Omega$  do
5:
6:     — — —                                                ▷ Update the reference ray
7:      $\mathbf{k} \leftarrow k \mathbf{k} / |\mathbf{k}|$                             ▷ Normalise the ray direction
8:      $q_{\mathbf{x}} = \mathbf{k}/k$                                     ▷ Compute the update variables
9:      $q_{\mathbf{k}} = \nabla k(\mathbf{x})$ 
10:     $\mathbf{k}' \leftarrow \mathbf{k} + \Delta s q_{\mathbf{k}}$                     ▷ Update the auxiliary ray direction
11:     $k' \leftarrow k(\mathbf{x} + \Delta s q_{\mathbf{x}})$                 ▷ Update the auxiliary wavenumber
12:     $\mathbf{k}' \leftarrow k' \mathbf{k}' / |\mathbf{k}'|$                     ▷ Normalise the auxiliary ray direction
13:     $q'_{\mathbf{x}} = \mathbf{k}'/k'$                                 ▷ Compute the auxiliary update variables
14:     $q'_{\mathbf{k}} = \nabla k(\mathbf{x} + \Delta s q_{\mathbf{x}})$ 
15:     $\mathbf{x} \leftarrow \mathbf{x} + (\Delta s/2)(q_{\mathbf{x}} + q'_{\mathbf{x}})$         ▷ Update the ray position
16:     $\mathbf{k} \leftarrow \mathbf{k} + (\Delta s/2)(q_{\mathbf{k}} + q'_{\mathbf{k}})$         ▷ Update the ray direction
17:
18:     — — —                                                ▷ Update the paraxial ray: amplitude
19:      $q_{\delta\mathbf{x}} = \delta\mathbf{k}/k$                                 ▷ Compute the update variables
20:      $q_{\delta\mathbf{k}} = \left( \frac{1}{k^2} \nabla k \nabla k^T + \frac{1}{k} \nabla^2 k \right) \delta\mathbf{x}$ 
21:      $\delta\mathbf{k}' \leftarrow \delta\mathbf{k} + \Delta s q_{\delta\mathbf{k}}$             ▷ Update the auxiliary ray direction perturbation
22:      $\delta\mathbf{x}' \leftarrow \delta\mathbf{x} + \Delta s q_{\delta\mathbf{x}}$             ▷ update the auxiliary ray position perturbation
23:      $q'_{\delta\mathbf{x}} = \delta\mathbf{k}'/k'$                             ▷ Compute the auxiliary update variables
24:      $q'_{\delta\mathbf{k}} = \left( \frac{1}{k'^2} \nabla k' \nabla k'^T + \frac{1}{k'} \nabla^2 k' \right) \delta\mathbf{x}'$ 
25:      $\delta\mathbf{x} \leftarrow \delta\mathbf{x} + (\Delta s/2)(q_{\delta\mathbf{x}} + q'_{\delta\mathbf{x}})$     ▷ Update the ray position perturbation
26:      $\delta\mathbf{k} \leftarrow \delta\mathbf{k} + (\Delta s/2)(q_{\delta\mathbf{k}} + q'_{\delta\mathbf{k}})$     ▷ Update the ray direction perturbation
27:
28: end while
    
```

---

*Grid-to-ray interpolation:* The wavenumber field is updated on the grid points, so for implementing algorithm 1, it must be interpolated onto the rays' sampled points. Here, the grid-to-ray interpolation was performed using a B-spline interpolation, which provides continuous values for  $\nabla k$  and  $\nabla^2 k$  at any arbitrary (offgrid) point. (For further details, see [1].)

## 5. RAY COORDINATES

In general, for the 2D case, the coordinates of the ray are given by two parameters: one specifying the initial direction of the ray and another a monotonic parameter along the ray [34]. Here, the ray parameters are chosen the angle component of the initial direction in the polar coordinate,  $\theta$ , and the arc length  $s$ .

*Definition 1.* The trajectory of a ray linking an emission point  $e$  to a reception point  $r$  is defined by the points with arc lengths  $s_m$ ,  $m \in \{0, \dots, M_{(e,r)}\}$ . Therefore, the points are initialised from  $s_0$  with  $\mathbf{x}(s_0) := \mathbf{x}_e$ , and are terminated at the point  $s_{M_{(e,r)}}$  with  $\mathbf{x}(s_{M_{(e,r)}}) := \mathbf{x}_r$ , the position of receiver  $r$ . The points  $s_m$  satisfy

$$s_m = \begin{cases} m\Delta s, & m \in \{0, \dots, M_{(e,r)} - 1\} \\ (m-1)\Delta s + \Delta s', & m = M_{(e,r)}. \end{cases} \quad (42)$$

Here, the second line is used in order to indicate that the last point of the ray must be matched to the reception point  $r$ , and therefore  $\Delta s' = s_{M_{(e,r)}} - s_{M_{(e,r)}-1}$  with  $\Delta s' \leq \Delta s$  [41].

*Definition 2.* For each excitation  $e$ , the pressure field is approximated on a set of linked rays  $f_{(k, \mathbf{x}_r; \mathbf{x}_e)} = 0$ . These rays are parameterised in space using  $\mathbf{x}(s_m, \theta_{(r,e)})$ , which denotes the position on the arc length  $s$  of the point  $m$  along a ray linking the emission position  $\mathbf{x}_e$  to the reception position  $\mathbf{x}_r$ . Also, the polar initial direction of this ray is indicated by  $\theta_{(r,e)}$ .

Accordingly, the Green's function  $g(\mathbf{x}; \mathbf{x}_e)$  is discretised at the sampled points along the rays linking the emitter  $e$  to all receivers  $r$  using the coordinates defined in Definition 2 in the form

$$g(\mathbf{x}(s_m, \theta_{(r,e)}); \mathbf{x}_e) \approx A(\mathbf{x}(s_m, \theta_{(r,e)}); \mathbf{x}_e) \exp\left(i(\phi(\mathbf{x}(s_m, \theta_{(r,e)}); \mathbf{x}_e) + \pi/4)\right), \quad (43)$$

where  $\mathbf{x}_e := \mathbf{x}(s_0, \theta_{(r,e)})$ . Note that the procedure for discretisation of the inverse Green's functions  $g^\dagger(\mathbf{x}(s_m, \theta_{(r,e)}); \mathbf{x}_e)$  and  $g^\dagger(\mathbf{x}(s_m, \theta_{(e,r)}); \mathbf{x}_r)$  is the same. (cf. Eq. (32).) In (43), the accumulated phase  $\phi$  is approximated in the form

$$\phi(\mathbf{x}(s_m, \theta_{(r,e)}); \mathbf{x}_e) = \int_{s_0}^{s_m} k(\mathbf{x}(s_m, \theta_{(r,e)})) ds - \frac{\pi}{2} K(s_m, \theta(r, e)), \quad (44)$$

where  $K(s_m, \theta(r, e))$  is the cumulative times the sign of the ray Jacobian along the ray has been changed. Points on which the ray Jacobian changes sign are called *caustics*, and will lead to a  $\pi/2$  shift in the phase [34].

The contributions of the amplitude factor  $A$  from absorption is  $A_{abs}$ , and is computed in the form

$$A_{abs}(\mathbf{x}(s_m, \theta_{(r,e)}); \mathbf{x}_e) = \exp\left(-\int_{s_0}^{s_m} \alpha(\mathbf{x}(s_m, \theta_{(r,e)}); \mathbf{x}_e) ds\right). \quad (45)$$

The contributions of the amplitude factor  $A$  from the geometrical spreading,  $A_{geom}$ , is determined by the relative change of the ray Jacobian along the ray with respect to a reference point on which

the amplitude can be determined analytically [51]. Correspondingly, the Jacobian  $J$  on the point  $m$  along the ray initialised by angle  $\theta_{(r,e)}$  satisfies

$$J(s_m, \theta_{(r,e)}) = \det \Xi(s_m, \theta_{(r,e)}), \quad (46)$$

where  $\Xi$  is the *transformation matrix* from the ray coordinates  $\gamma = (\gamma_1, \gamma_2)^T$  to the general Cartesian coordinates  $\mathbf{x} = (\mathbf{x}_1, \mathbf{x}_2)^T$  with components

$$\Xi_{ij} = \frac{\partial x_i}{\partial \gamma_j}. \quad (47)$$

In general,  $\gamma_1$  must be a parameter specifying the ray, and  $\gamma_2$  must be a monotonic parameter along the ray. (See [34], section 3.10.) Here,  $\gamma_1 = \theta$  and  $\gamma_2 = s$ , as discussed in Definition 2. The geometrical attenuation  $A_{geom}$  now satisfies

$$A_{geom}(\mathbf{x}(s_m; \theta_{(r,e)}); \mathbf{x}_e) = \left( \frac{c(\mathbf{x}(s_m, \theta_{(r,e)}))}{c(\mathbf{x}(s_1, \theta_{(r,e)}))} \frac{J(s_1, \theta_{(r,e)})}{J(s_m, \theta_{(r,e)})} \right)^{1/2} A_{geom}(\mathbf{x}(s_1, \theta_{(r,e)}); \mathbf{x}_e), \quad (48)$$

where  $s_1$  is the next point after the initial point along the ray, and is chosen as the reference point, using an assumption that a neighborhood of the initial point of the rays with a radius greater than ray spacing  $\Delta s$  is acoustically homogeneous, and therefore,  $A_{geom}(\mathbf{x}(s_1, \theta_{(r,e)}); \mathbf{x}_e)$  can be calculated analytically [34].

## 6. NUMERICAL RESULTS

This section describes numerical experiments demonstrating the effectiveness of the proposed ray-based inversion approach for a low-cost computation of a high-resolution image of the sound speed distribution inside the breast.

**6.1. Data simulation.** An imaging system consisting of 64 emitters and 256 receivers uniformly distributed along a circular ring with radius  $R = 9.5\text{cm}$  was simulated. A horizontal slice of a 3D digital phantom, which mimics the acoustic properties of the breast and is freely available [52], was used in this study. The sound speed was set to a range  $1470\text{--}1580\text{ ms}^{-1}$ , and the absorption coefficient  $\alpha_0$  was set to a range  $0\text{--}1\text{ dBMHz}^{-y}\text{cm}^{-1}$ , and the power law exponent  $y$  was set to 1.4. Figures 1(a) and 1(b) show the maps for the sound speed and absorption coefficient of the breast phantom, respectively. The sound speed and absorption coefficient in water was set  $1500\text{ ms}^{-1}$  and 0, respectively. The computational grid consisted of  $502 \times 502$  grid points with position  $[-10.04, +10.00] \times [-10.04, +10.00]\text{cm}^2$  and a grid spacing of  $\Delta x = 4 \times 10^{-2}\text{cm}$  along all the Cartesian coordinates. Using this sound speed distribution and grid spacing, the maximum frequency supported by the grid,  $f_{\max}$ , was 1.84 MHz.

*Simulating time series data.* A *k-space pseudo-spectral* method (k-Wave) was used to simulate the acoustic pressure time series data on the detection ring via solving a system of three-coupled first-order wave equations equivalent to the Szabo's second-order wave equation, which is a time-domain variant of Eq. (2) with the wavenumber defined by (5) [39, 40, 54]. The emitters and receivers were assumed as points placed on the circle, and the interpolation of the pressure field between the grid and these transducers was performed using the *off-grid* toolbox [53]. To simulate the data, each emitter was individually driven by an excitation pulse, and the induced acoustic pressure time series were recorded at the receivers at 6466 time points with a sampling rate of 39.6MHz (25.25 ns time spacing). This was repeated for each emitter. Figure 2(a) shows the normalised amplitude of the excitation pulse (pressure source) in the time domain, and figure 2(b) shows the normalised

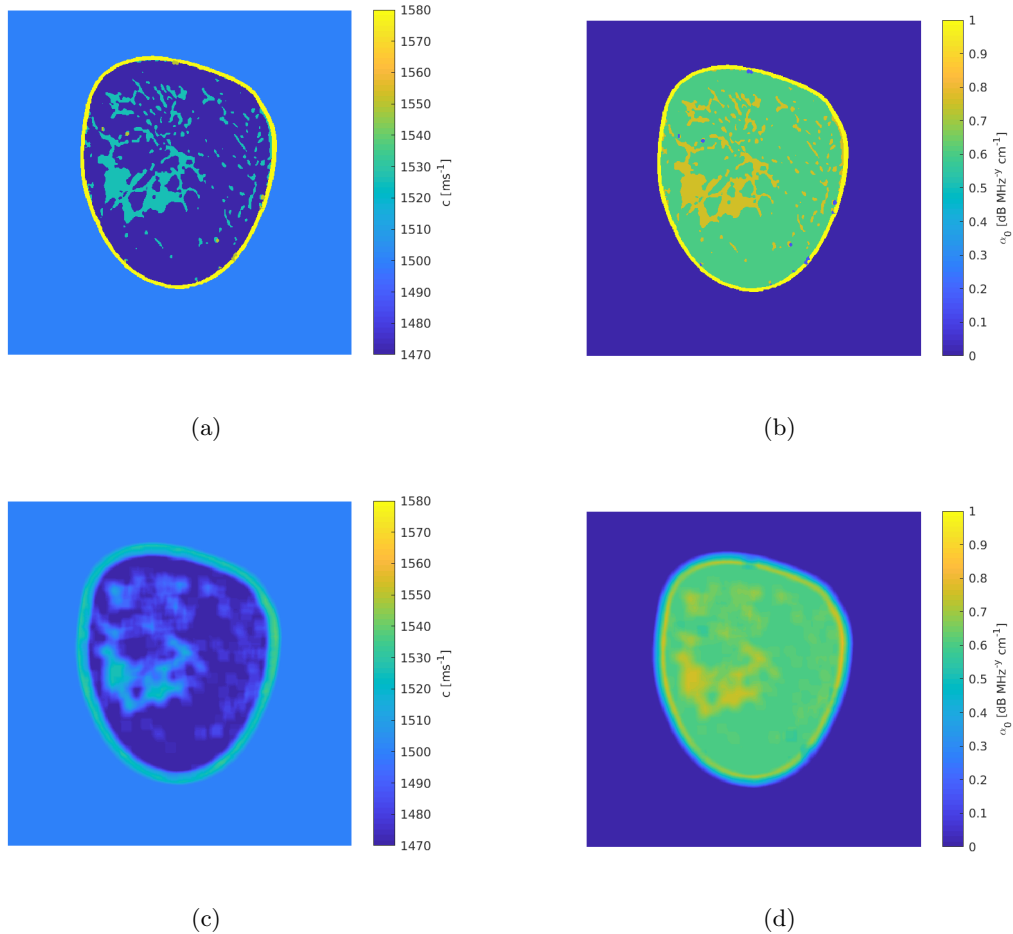


FIGURE 1. Phantom used for the simulation of synthetic UST data using the k-Wave toolbox: (a) sound speed [ $\text{ms}^{-1}$ ] (b) absorption coefficient [ $\text{dB MHz}^{-y}\text{cm}^{-1}$ ], (c) smoothed sound speed [ $\text{ms}^{-1}$ ], (d) smoothed absorption coefficient [ $\text{dB MHz}^{-y}\text{cm}^{-1}$ ]. The maps are shown on a grid consisting of  $502 \times 502$  points (used for the k-Wave simulation). The smoothed fields (c) and (d) are obtained by applying an averaging window of size 17 points on the original fields (a) and (b), respectively. The original (nonsmoothed) fields are used for simulating data used for image reconstruction, and the smoothed fields are used for simulating data used as a benchmark for comparison with the ray approximation to heterogeneous Green's function. The power law exponent was assumed  $y = 1.4$  and homogeneous.

amplitude and phase components of the excitation pulse in frequency domain, respectively. This signal is used as the pressure source for all excitations.

**6.2. Numerical validation of the ray approximation to the Green's function.** In this section, our approximate Green's function solution to Szabo's wave equation, proposed in section 2, numerically solved in section 4 and discretised in section 5, is compared to a full-wave solution using k-Wave [39, 40] in a heterogeneous and absorbing medium with a spatially smooth variations

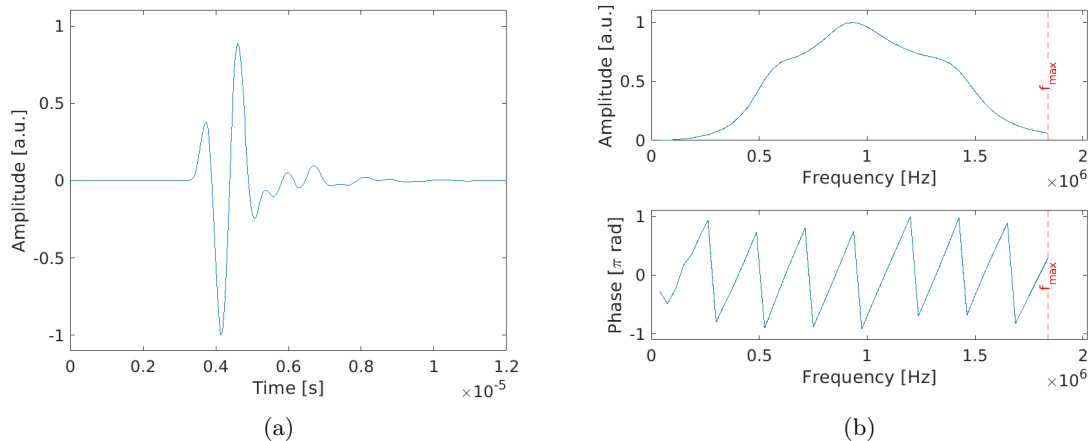


FIGURE 2. Excitation pulse used for all emitters: (a) time domain, (b) frequency domain: normalised amplitude and phase.  $f_{max}$  indicates the maximum frequency supported by the grid used for the k-Wave simulations.

in acoustic properties. Further details about derivation of the Green’s function solution to Szabo’s wave equation have been given in [1]. For the k-Wave simulation, emitter 1 is excited by the excitation pulse shown in figures 2(a) and 2(b), and the induced pressure propagates across the breast in water, and is recorded on all the 256 receivers. The Green’s function  $p(\omega; \mathbf{x}_r; \mathbf{x}_e)$  depends only on the accumulated information and geometrical spreading along the linked rays, and does not include the scattering effects. Therefore, the scattering effects were minimised in the k-Wave simulation by applying an averaging window of size 17 grid points on the sound speed and absorption coefficient fields. The smoothed variant of the sound speed and absorption coefficient maps are shown in figures 1(c) and 1(d).

For the ray-approximation approach, the Green’s function was approximated using (43) along the linked rays, as described in section 5. Following Eq. (6), the computed Green’s function was used for approximating the pressure time series on the receivers after being produced by the emitter 1. In the image reconstruction below, the inverse crime was avoided by using two different computational grids for data simulation and image reconstruction. (Note that using different grids may not be necessary in our study, because two inherently different approaches are used for the data simulation and image reconstruction.) For image reconstruction below, the computational grid has a size  $200 \times 200$  points with a grid spacing of 1 mm. Therefore, the ray approximation to the Green’s function used for comparison with the k-Wave simulation was also performed on the same grid. For implementing the ray approximation to the Green’s function, the smoothed sound speed and absorption coefficient fields used for the k-Wave simulation were interpolated onto the grid for image reconstruction, and the resulting wavenumber field was smoothed by an averaging window of size 7 points for minimising the interpolation effects. (Compared to the grid for k-Wave simulation, the averaging window size was reduced reciprocally to the increase in the grid spacing along each Cartesian coordinate.) The pressure field emanated from emitter 1 was approximated on all the 256 receivers at a single frequency 1 MHz and for three cases: only water, non-absorbing breast and absorbing breast inside water.

Figure 3(a) shows the phase of the pressure time series on all the receivers after being produced by emitter 1. (The phases were wrapped to  $[-\pi, \pi]$ .) The green plot shows the phases which are

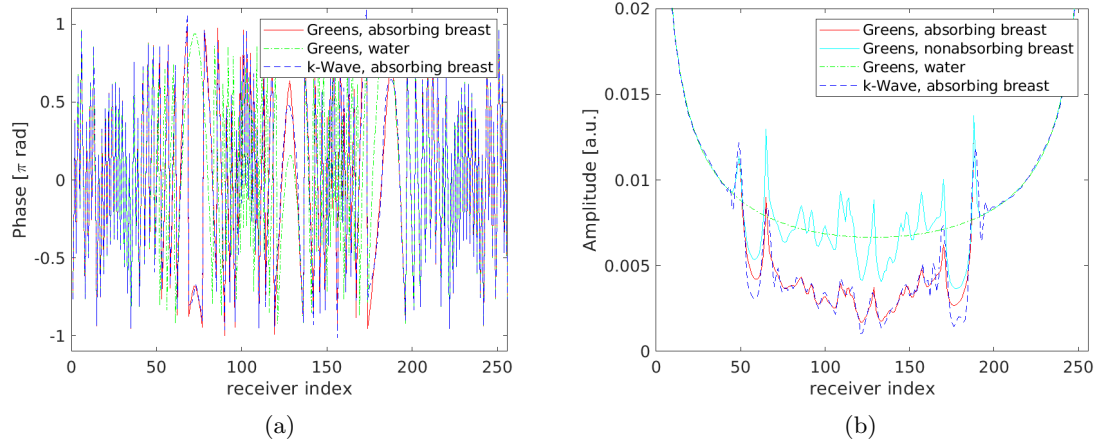


FIGURE 3. The pressure time series on all the receivers at single frequency 1 MHz after being produced by emitter 1: (a) phase, (b) amplitude.

analytically computed by the homogeneous Green's function by assuming only water, and the red plot shows the phases computed using the ray approximation to the Greens function propagated through the absorbing breast inside water. (cf. Eq. (44).) Also, the phase of the pressure time series simulated by k-Wave for the absorbing breast inside water was shown by the blue plot. As shown in this figure, for receivers in the range 50-180, for which the linked rays travel through the breast (not only water), the ray approximation to the heterogeneous and absorbing Green's function and the k-Wave simulation have very good agreement, but the Green's function analytically calculated by assuming only water has large discrepancies with the k-Wave.

Figure 3(b) shows the amplitude of the pressure time series on all the receivers after being produced by emitter 1. The green plot shows the amplitudes computed by the analytic Green's function by assuming only water. The amplitudes computed using the Green's function by assuming a nonabsorbing breast, i.e., the amplitudes attenuated by only the geometrical spreading, were approximated on all the receivers using (48), and are shown by the light blue plot. It is reminded that for computing (48), the rays' Jacobian was approximated using paraxial ray tracing, as discussed in section 4. The amplitudes computed using the Green's function propagated through the absorbing breast were approximated as the product of the amplitude decay from geometrical spreading (the light blue plot) and the accumulated acoustic absorption, and are shown by the red plot. The accumulated acoustic absorption was computed using (45). The amplitudes of the pressure time series simulated by k-Wave and recorded on all the receivers are shown by the dark blue plot. As shown in this figure, for the absorbing breast, the amplitudes computed by the product of the geometrical spreading using paraxial ray tracing and the accumulated acoustic absorption have very good agreement with the amplitudes computed by the k-Wave, but the analytically calculated Green's function assuming only water or the Green's function neglecting the acoustic absorption have large discrepancies with the k-Wave.

**6.3. Image reconstruction.** This section explains the procedure for image reconstruction from the ultrasound data simulated by k-Wave, and shows the reconstructed images. The k-Wave was used for simulating two sets of synthetic data, as described in section 6.1. The first data set was simulated for only water, and the second data set was simulated for the digital breast phantom inside

water. The breast-in-water data was simulated using the sound speed and absorption coefficient maps shown in figures 1(a) and 1(b), respectively. For producing each data set, each emitter is excited by the excitation pulse shown in figures 2(a) and 2(b), and the induced pressure time series were recorded on all the receivers. The excitation and measurements were sequentially repeated for all the emitters. The computational time for simulation of the UST data set including all the excitations for the digital breast phantom inside water using k-Wave’s Matlab code [39] on a single 8-core Xeon E5-2620 v4 2.1 GHz CPU was about 5 hours. Different levels of additive white Gaussian noise (AWGN) were added to the simulated pressure time series to provide 40 dB, 30 dB and 25 dB signal-to-noise ratio (SNR) of the peak amplitudes for both breast-in-water and only-water data sets.

For reducing an inverse crime in time spacing, the time series simulated by k-Wave on the receivers were temporally downsampled by 2 before image reconstruction. Also, the grid for image reconstruction consisted of  $200 \times 200$  grid points with position  $[-10.1650, +10.1350] \times [-10.1650, +10.1350]\text{cm}^2$  and a grid spacing of  $\Delta x = 1\text{mm}$  along all the Cartesian coordinates. The image reconstruction was performed on the grid points inside a binary mask with radius 0.95 of the radius of the detection ring. Because the sound speed is reconstructed on the grid points, the parameters of Green’s function, which are approximated along the linked rays, must be interpolated onto the grid points. The interpolation of the computed parameters of the Green’s function on the linked rays onto the grid points are done by enforcing a triangulation on the sampled points on the linked rays, and then interpolating the approximated parameters of Green’s functions on the rays’ points onto the grid points using a trilinear interpolation. The linked rays initialised from emitters are also used for computing the Green’s functions emanated from receivers. This was done by reversing the accumulated parameters along the linked rays [1]. (In the formulae in section 5, this is equivalent to replacing  $e$  and  $r$ .) Note that for approximating the geometrical portion of the amplitudes for  $g^\dagger(c; \mathbf{x}; \mathbf{x}_r)$ , an additional paraxial ray must be traced along each reversed ray.

6.3.1. *Inversion approach using time-of-flights (initial guess).* Because the objective function in (9) is highly nonlinear, an initial guess is often used [13, 14, 15, 17, 18, 19]. Here, an image reconstruction approach based on the direct time of flight (TOF) of the measured (simulated) pressure time series was used to provide an initial guess. The TOF-based inversion approach iteratively minimises the norm of discrepancy between the TOFs obtained from the measured (simulated) pressure time series using a first-arrival picking algorithm and the TOFs modelled by the ray tracing algorithm (the first part of Algorithm 1) [10]. The effects of measurement errors on the picked first-arrivals are compensated for using a difference inversion approach, in which the difference of the sound speed between the breast in water and only water is computed from the discrepancy of the first-arrival times picked from the measured breast-in-water and only-water data sets. The minimisation is performed by iteratively linearising the associated objective function, and solving the arising linearised subproblems using a Radon-type technique. Here, each linearised subproblem was solved using a Simultaneous Algebraic Reconstruction Technique (SART) algorithm, which accounts for the nonuniform ray density across the image due to the curved nature of the rays [56]. For computing rays’ trajectories at each linearisation, the sound speed update was smoothed by an averaging window of size 7 grid points, but integration of accumulated time-of-flights along trajectory of the linked rays are performed on the nonsmooth updates, i.e., the constructed system matrix was multiplied by the nonsmoothed sound speed update. The ray linking was performed using the Secant method such that for each emitter-receiver pair, the linked ray (optimal ray after ray linking) at each linearisation is used as the initial guess for ray linking at the next linearisation [41, 1]. The TOF-based algorithm was terminated after few linearisations to

provide a good trade-off between accuracy and the artefact due to the error in the picked first-arrival times [1].

6.3.2. *Inversion approaches using ray approximation to heterogeneous Green’s function.* Below, the procedure for implementing the inversion approach based on the Green’s function is explained. For evaluating the effectiveness of the proposed inversion approach, the approach used in [1] was used as the benchmark. The image reconstruction is equivalent to computing the sound speed distribution  $c$  which minimises the objective function (9). To achieve this aim, the objective function is discretised at a number of frequencies within the frequency range of the transducers, and is minimised from low to high frequencies until the computed update direction becomes smaller than a tolerance. For computing the residual (10), the measured Green’s function  $\hat{g}_{(\omega,r;e)}$  is derived by deconvolving the excitation pulse from the measured (simulated) pressure time series. Here, the deconvolution was performed using a Tikhonov regularised inversion approach in the frequency domain [55]. Also, the Green’s functions  $g_{(c;\omega,\mathbf{x}_r;\mathbf{x}_e)}$  were approximated along the linked rays computed on the last update of the sound speed.

*Ray linking.* For both the TOF-based and the Green’s function-based approaches, the ray linking was performed on the updates of the sound speed for all emitter-receive pairs separately. For each update of the sound speed and each emitter-receiver pair, the ray linking was done by iteratively updating the initial unit direction of the ray using a Secant method [1, 41, 50]. The initial guess for the unknown initial unit direction of the ray was set the obtained optimal initial direction after ray linking for the last previous update of the sound speed, and the ray’s trajectory is iteratively computed using the first part of Algorithm 1 until the interception point of the ray by the detection ring matches the position of the reception point within a tolerance. The parameters of Green’s functions are then computed along the linked rays using the formulae given in section 5. For computing the geometrical portion of the amplitude, the linked ray is used as the reference ray, and a paraxial ray is computed via implementing the second part of Algorithm 1. For computing the rays’ trajectories through ray linking, an averaging window of size 7 grid points was applied on the updated wavenumber fields, but the nonsmoothed updates were used for integration along the rays and approximating the Green’s functions using the formulae in section 5.

a) *Hessian-inversion-free ray-born inversion.* The inversion approach described in section 3 was implemented at 140 discretised frequencies in the range  $f \in \{0.2, \dots, 1.5\}$  MHz. The image reconstruction was performed from low to high frequencies such that each update of the sound speed was computed at two consecutive discretised frequencies using Eq. 30. ( $n \in \{1, \dots, 70\}$ .) For each linearisation, in addition to the Green’s functions  $g(\omega; \mathbf{x}_r; \mathbf{x}_e)$  included in the residual, the inverse Green’s functions  $g^\dagger(\omega; \mathbf{x}; \mathbf{x}_e)$  and  $g^\dagger(\omega; \mathbf{x}; \mathbf{x}_r)$  are computed on the forward and backward rays, which are the rays initialised from emitters  $e$  and  $r$ , respectively. The step length was heuristically chosen  $\tau = 3 \times 10^{-10}$  for all linearisations. The major portion of the computational cost for solving each linear problem (13) is ray tracing, because the update direction is obtained in one step using (30). Therefore, using this approach, the computational cost for solving each linearised subproblem is almost the same as each linearised subproblem in the TOF-based algorithm. Note that the total number of linearisations for reaching an optimal point using this approach was almost five times more than the TOF-based algorithm.

b) *Hessian-inversion-based ray-born inversion (Gauss-Newton).* Using  $\mathcal{Q} = I$ , where  $I$  is an identity matrix, in the objective function (9) and its linearised variant (11), each arising linearised subproblem  $n$  (13) is solved by first forming the gradient  $\nabla \mathcal{F}^{(n)}$  and then computing the update direction via iteratively computing the action of the Hessian matrix  $H^{(n)}$  on the updates

of perturbation to the sound speed. This is equivalent to computing a Gauss-Newton search direction. The reader is referred to [1] for further details. Here, each linearised subproblem was solved using 10-15 inner iterations. Note that early stopping the inner iterations has regularising effects on the solution. For providing a benchmark for evaluating the performance of the proposed Hessian-inversion-free ray-born inversion algorithm, the Gauss-Newton inversion approach described in [1] was implemented at 100 discretised frequencies in the range  $f \in \{0.2, \dots, 1.1\}$  MHz. Like the Hessian-inversion-free approach, the image reconstruction was performed from low to high frequencies such that each update of the sound speed was computed at two consecutive discretised frequencies. ( $n \in \{1, \dots, 50\}$ .) Compared to the Hessian-inversion-free approach, the algorithm was terminated at smaller  $n$ , because solving linearised subproblems at frequencies larger than 1.1 MHz provides very small search directions. Note that as described in section 4, the geometrical portion of the amplitude was computed via solving a paraxial system of equations. (cf. Algorithm 1.) The step length was heuristically chosen  $\tau = 3 \times 10^{-2}$  for all linearisations. Using our developed code in a Matlab environment using the CPU mentioned in the first paragraph in section 6.3, the computational time for solving each linearised subproblem  $n$  and computing each Gauss-Newton search direction was almost an order of magnitude more than solving each linearised subproblem using the proposed Hessian-inversion-free approach. Compared to the full-wave inversion, the total computational time for reconstructing an image using the Gauss-Newton algorithm was almost the same as the computational time for simulating the breast-in-water UST data using k-Wave, i.e., solving a single forward problem using k-Wave.

**6.4. Reconstructed images.** In this section, the sound speed images reconstructed using the proposed Hessian-inversion-free ray-born inversion approach are shown, and are compared to the images reconstructed using the Gauss-Newton inversion approach [1]. The reconstructed images are evaluated in terms of Relative Error (RE), i.e.,

$$RE_{\text{image}} = \frac{\|c_{\text{image}} - c_{\text{phantom}}\|_2}{\|c_{\text{water}} - c_{\text{phantom}}\|_2} \times 100, \quad (49)$$

where  $c_{\text{phantom}}$  and  $c_{\text{image}}$  are the stack-vectors of the sound speed of the digital breast phantom interpolated onto the grid for image reconstruction and the reconstructed sound speed image, respectively. These stack-vectors are obtained on the grid points inside the binary mask for image reconstruction. Also,  $c_{\text{water}} = 1500 \text{ ms}^{-1}$ , and is the speed of sound in water. (cf. section 6.1.)

*6.4.1. Reconstructed images from UST data with high SNR.* Below, the reconstructed sound speed images from the synthetic data with a high signal-to-noise ratio (SNR) are shown, and are evaluated in terms of RE. Figure 4(a) shows the sound speed map of the digital breast phantom (ground truth). Figure 4(b) shows the image reconstructed from time-of-flights of the time-series with 40 dB SNR. Following [10], the time-of-flights were computed using a modified Akaike-Information-Criterion (AIC) approach.

As described in section 2, the proposed forward model based on the ray approximation to heterogeneous Green's function can account for the acoustic absorption and dispersion, but the absorption coefficient  $\alpha_0$  map and the exponent power  $y$  are not known in a practical setting. Here, the exponent power was assumed known and set  $y = 1.4$ , and the image reconstruction was performed using three assumptions: known  $\alpha_0$  map (figure 1(b)), zero  $\alpha_0$ , and a homogeneous  $\alpha_0$  which can be determined in a practical setting from the mean logarithmic relative change of the amplitudes of the measured time series for the breast-in-water and only-water data sets. (Here, the homogeneous absorption coefficient was set  $0.5 \text{ dBMHz}^{-y} \text{ cm}^{-1}$ .)

Figures 4(c) and 4(d) show the reconstructed sound speed images from the 40dB-SNR synthetic data using an assumption that  $\alpha_0$  map is known and using the Gauss-Newton and the proposed Hessian-inversion-free ray-born inversion approaches, respectively. In the same way, figures 4(e) and 4(f) show the reconstructed images using the assumption that  $\alpha_0 = 0$ , i.e., the acoustic absorption and dispersion are neglected. Also, figures 4(g) and 4(h) show the reconstructed images when the absorption coefficient map was assumed  $\alpha_0 = 0.5 \text{ dBMHz}^{-y}\text{cm}^{-1}$  and homogeneous inside the breast. The RE of the reconstructed images are written in the caption of the figure.

As shown in this figure, the images reconstructed by the proposed Hessian-inversion-free approach (right column) are slightly smoother than the images reconstructed using the Gauss-Newton inversion approach (left column). The smoothness effects are because of the two smoothness approximations made in Eqs. (20) and (21). For the high-SNR UST data used in this experiment, the images reconstructed using the Gauss-Newton inversion approach are more accurate than those reconstructed by the Hessian-inversion-free approach in terms of RE. This suggests that the Gauss-Newton approach, which is based on an implicit and iterative inversion of the full Hessian matrix, is more accurate than the proposed Hessian-inversion-free approach for high-SNR data.

Furthermore, an assumption of zero  $\alpha_0$  has led to less accuracy and more artefact for the reconstructed images, but assuming homogeneous  $\alpha_0$  for the breast has provided images almost the same as those reconstructed using an assumption of true and known  $\alpha_0$  in terms of RE. It is reminded that the exponent power was assumed known for both cases.

6.4.2. *Reconstructed images from UST data with medium and low SNR.* Below, the reconstructed images from simulated ultrasound data with medium and low SNR and using an assumption of homogeneous  $\alpha_0 = 0.5 \text{ dBMHz}^{-y}\text{cm}^{-1}$  are presented. Accordingly, figures 5(a) and 5(b) show the TOF-based images computed from the UST synthetic data with 30 dB and 25 dB SNR, respectively. Figures 5(c) and 5(d) show the images reconstructed using the Gauss-Newton inversion approach and from the UST data with 30 dB and 25 dB SNR, respectively. In the same way, figures 5(e) and 5(f) show the images reconstructed using the proposed Hessian-inversion-free approach. As shown in figures 5(a)-5(d), an increase in the additive white Gaussian noise in the UST data have led to more artefact and more RE in the TOF-based reconstructed images (initial guesses) and the images reconstructed using the Gauss-Newton inversion approach. Additionally, figures 5(e) and 5(f) show that the proposed Hessian-inversion-free ray-born inversion approach has reconstructed images with less artefact than the Gauss-Newton inversion approach from the UST data with 30 dB and 25 dB SNR. For the data with 25 dB SNR, the sound speed image reconstructed using the Hessian-inversion free approach is more accurate than the Gauss-Newton approach in terms of RE.

Figures 6(a), 6(b) and 6(c) show the reconstructed quantities of the sound speed along the main diagonal of the grid for image reconstruction from UST data with 40 dB, 30 dB and 25 dB SNR, respectively. The quantities of the sound speed for the digital breast phantom interpolated from the grid for the k-Wave data simulation onto the grid for image reconstruction are shown by the black colour, the quantities reconstructed using early iterations of the TOF-based approach are shown by the blue colour, and the quantities reconstructed using the Gauss-Newton and the proposed Hessian-inversion-free approaches are shown by the green and red colours, respectively. As shown in figures 6(b) and 6(c), for the UST data with medium and low SNR, some erroneous quantities smaller than the background quantity of the breast ( $1570 \text{ ms}^{-1}$ ) have appeared in the plot for the image reconstructed using the Gauss-Newton approach (green plot), but those incorrect values have not appeared in the plots obtained using the Hessian-inversion-free approach (red plot). The erroneous quantities in figures 6(b) and 6(c) have appeared as artefact in the reconstructed images shown in figures 5(c) and 5(d), respectively.

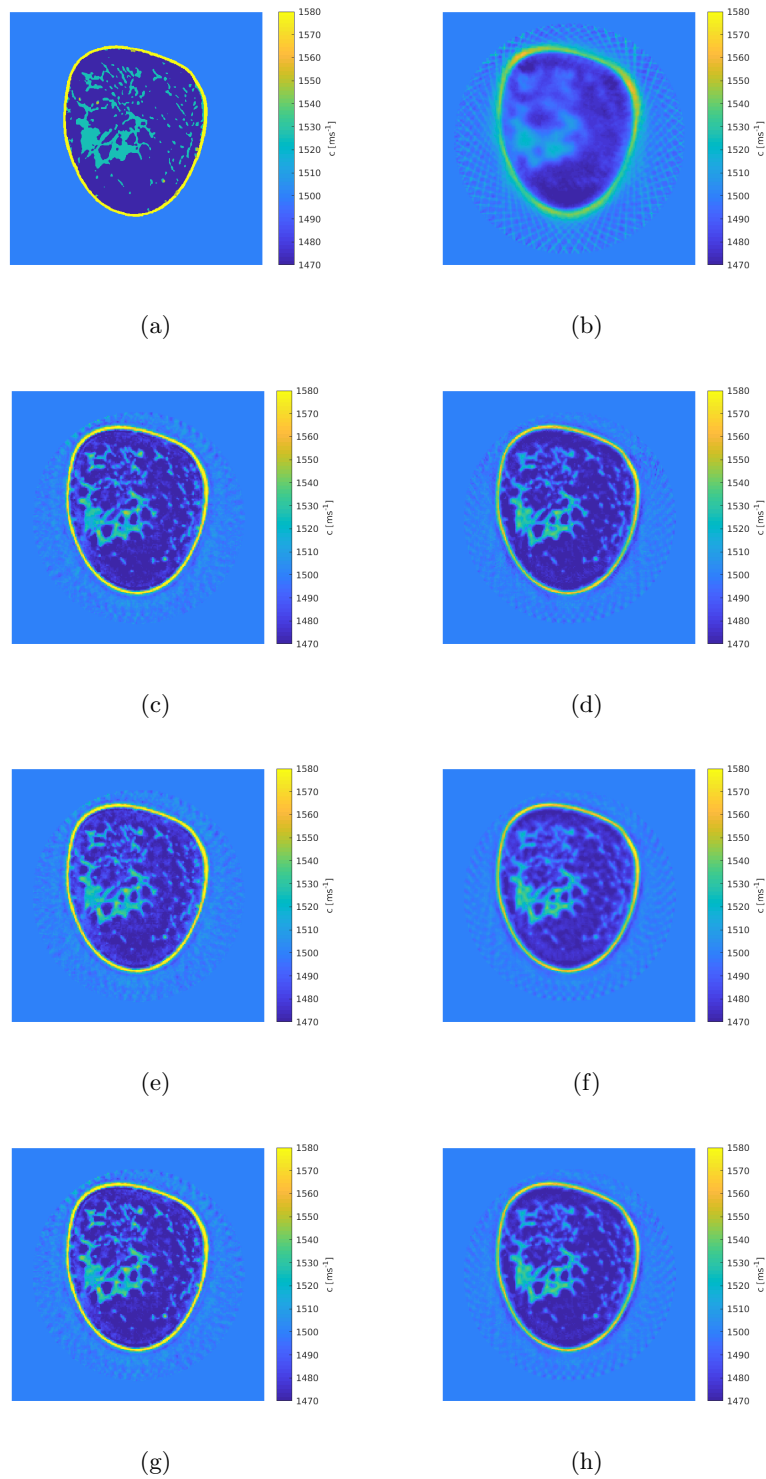


FIGURE 4. (a) Ground truth, Reconstructed sound speed images from UST data with 40dB SNR: (b) Time-of-flight-based approach (initial guess),  $RE = 73.4\%$ . True  $\alpha_0$  (Figure 1(b)): (c) Gauss-Newton,  $RE = 37.3\%$ , (d) Hessian-inversion-free,  $RE = 45.8\%$ .  $\alpha_0 = 0$ : (e) Gauss-Newton,  $RE = 39.9\%$ , (f) Hessian-inversion-free,  $RE = 48.6\%$ .  $\alpha_0 = 0.5 \text{ dB/MHz}^{-y}\text{cm}^{-1}$  (homogeneous inside breast): (g) Gauss-Newton,  $RE = 37.7\%$  (h) Hessian-inversion-free,  $RE = 45.81\%$ .

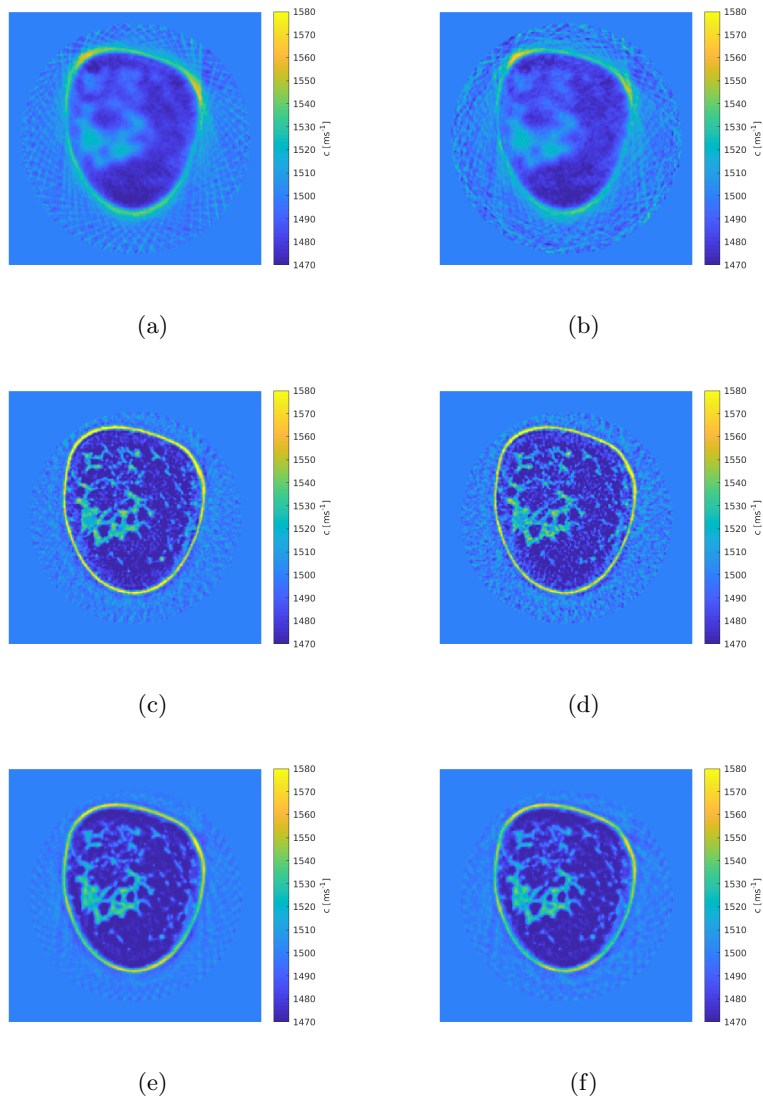


FIGURE 5. Reconstructed images using Time-of-flight-based approach (initial guess): (a) 30 dB,  $RE = 76.4\%$ , (b) 25 dB,  $RE = 80.2\%$ , Gauss-Newton: (c) 30 dB,  $RE = 44.9\%$ , (d) 25 dB,  $RE = 51.9\%$ , Hessian-inversion-free: (e) 30 dB,  $RE = 47.3\%$ , (f) 25 dB,  $RE = 49.6\%$ . The absorption coefficient map of the breast was assumed homogeneous and  $\alpha_0 = 0.5 \text{ dBMHz}^{-y}\text{cm}^{-1}$ .

This means that although the computational cost of the proposed Hessian-inversion-free inversion approach is almost an order of magnitude less than the Gauss-Newton approach, the proposed Hessian-inversion-free approach is more stable than the Gauss-Newton approach to noise.

## 7. DISCUSSION

This paper proposed an efficient approach for high-resolution and quantitative reconstruction of the sound speed of the breast from ultrasound time series. The propagation of acoustic waves

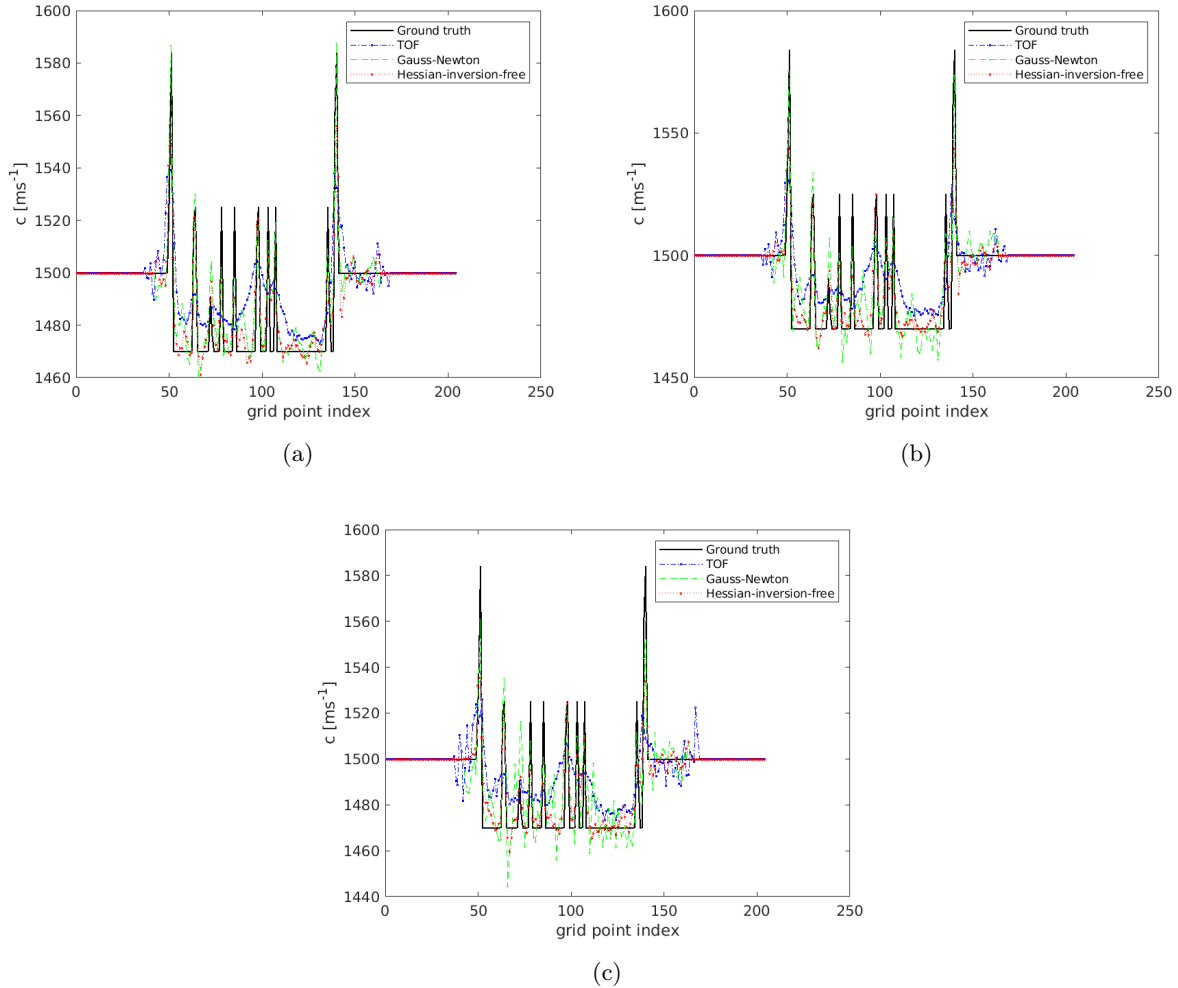


FIGURE 6. The reconstructed quantities of the sound speed along the main diagonal of the grid for image reconstruction from ultrasound data with: a) 40 dB SNR, b) 30 dB SNR, and c) 25 dB SNR. The absorption coefficient map of the breast was assumed homogeneous and  $\alpha_0 = 0.5 \text{ dBMHz}^{-y} \text{cm}^{-1}$ .

is modelled using Green’s function whose aberrations in the amplitude and phase because of heterogeneity of acoustic properties, refraction, geometrical spreading, and acoustic absorption and dispersion, are accounted for. The geometrical spreading due to changes in the area of ray tube is computed via solving a paraxial system of equations along the linked rays using Algorithm 1, as described in section 4. The proposed ray-based inversion approach can reconstruct a high-resolution image of the breast via including the first-scattered waves in the image reconstruction, considering that the higher-scattered waves are attenuated via acoustic absorption, and are buried in noise in a practical setting. (An inclusion of higher-scattered waves in an inversion approach based on the ray theory is possible, but it dramatically increases the computational cost.) The proposed inversion approach is in contrast with other Born and distorted Born inversion approaches used in medical UST, because these approaches neglect the heterogeneity of the medium

in modelling the Green’s function, and only includes the heterogeneity in the scattering potential [21, 22, 23, 24, 25, 26, 27, 28, 29, 30, 31]. Figures 3(a) and 3(b) show that neglecting the acoustic heterogeneity in computing the Green’s function leads to large errors in approximation of the phase and amplitude. In [32], an image reconstruction approach which combines the diffraction tomography with ray tracing on an ad-hoc basis was performed on a fixed background medium reconstructed using a TOF-based inversion approach. However, the procedure taken for image reconstruction is not derived from the common optimisation approaches.

Here, following [1], the objective function was iteratively linearised and solved in the frequency domain. Each linearisation was performed at a fixed number of consecutive discretised frequencies, here 2. The linearisations were sequentially done from low to high frequencies until the computed update directions become sufficiently small. In general, each linear subproblem (13) can be solved via an implicit and iterative inversion of the Hessian matrix using a linear minimisation algorithm. In [1] conjugate gradient (CG) algorithm was used. Instead, this manuscript proposed a preconditioning approach, in which the Hessian matrix is diagonalised with the aid of the smoothness assumptions (20) and (21), and is thus inverted in a single step.

The total computational cost of the Gauss-Newton inversion approach, which solves the linear subproblems via an implicit and iterative inversion of the hessian matrix, was almost the same as the computational cost for the k-Wave simulation for producing the breast-in-water data set, i.e., solving one forward problem of the full-wave inversion. Furthermore, the proposed Hessian-inversion-free inversion approach was computationally about an order of magnitude faster than the Gauss-Newton inversion approach, because the linear subproblem associated with each frequency set is solved in a single step using (30) and (31). In addition, the smoothness assumptions (20) and (21) significantly improved the stability of image reconstruction against noise. For UST data with 30 dB and 25 dB SNR, the proposed Hessian-inversion-free inversion approach reconstructed sound speed images with lower artefact than the Gauss-Newton inversion approach.

Our proposed forward model accounts for acoustic absorption and dispersion via solving a lossy Helmholtz equation based on the Szabo’s wave equation, but the map of acoustic absorption coefficient is not known in a practical setting. It was shown that the images reconstructed using an assumption of homogeneous absorption coefficient for the breast are almost as accurate as the images reconstructed using an assumption of the known and true absorption coefficient.

#### DATA AVAILABILITY STATEMENT

The data and Matlab codes that support the findings of this study, as well as the data for studies [1] and [41], will be available publicly. A GitHub link will be provided for the Matlab codes in the final version of this manuscript.

#### APPENDIX. A MODIFICATION TO THE K-WAVE FOR SIMULATION OF THE TIME-DEPENDENT SOURCE

A k-space method for solving the coupled first-order differential equations for propagation of acoustic waves in heterogeneous media was proposed in [54]. As discussed in section 6, an open-source toolbox for a numerical implementation of this approach was used in this study in order to simulate the UST pressure data recorded on the receivers [39, 40, 57]. Here, the procedure taken for simulation using the k-Wave is explained for lossless medium. (An inclusion of the acoustic absorption and dispersion in the simulation is straightforward.) To simulate acoustic waves for lossless media, the coupled first-order partial differential equations are defined in terms of the

excitation pulse  $s(\mathbf{x}, t)$  in the form

$$\begin{aligned}\frac{\partial}{\partial t}\mathbf{u}(\mathbf{x}, t) &= -\frac{1}{\rho_0}\nabla p(\mathbf{x}, t) \\ \frac{\partial}{\partial t}\boldsymbol{\rho}(\mathbf{x}, t) &= -\rho_0\nabla\mathbf{u}(\mathbf{x}, t) + \int_0^t s(\mathbf{x}, t') dt' \\ p(\mathbf{x}, t) &= c(\mathbf{x})^2\boldsymbol{\rho}(\mathbf{x}, t),\end{aligned}\tag{50}$$

where  $p$  is the scalar acoustic pressure, and  $\boldsymbol{\rho}$  and  $\mathbf{u}$  denote the vectors of acoustic density and particle velocity, respectively. Also,  $\rho_0$  is the ambient density and is assumed homogeneous. In (50), an assumption  $\int_0^{T_s} s(\mathbf{x}, t) dt = 0$  has been used. The second term in the right-hand-side of the second line is the mass source  $s_M$ , which represents the time rate of the input of mass per unit volume in units of  $\text{kgm}^{-3}\text{s}^{-1}$ , and satisfies

$$s(\mathbf{x}, t) = \frac{\partial s_M(\mathbf{x}, t)}{\partial t}.\tag{51}$$

**Numerical Implementation.** To take into account Eq. (51) for a given time-dependent excitation pulse  $s(\mathbf{x}, t)$ , the user must take a temporal integration from the excitation pulse, in which a scaling factor  $c_0 \Delta t/(2\Delta x)$  is enforced on the amplitude for accounting for the time spacing associated with the temporal integration of a cylindrically propagating isotropic source. The off-grid toolbox is then used for interpolating the mass source from the off-grid emission point onto the grid, and then the input *source* in the k-Wave is specified. Here,  $\Delta t$  and  $\Delta x$  are the time spacing and the spacing of the grid for the k-Wave simulation, respectively. Note that this integration must not be confused with an inclusion of the mass source in the numerical integration of the acoustic density using the same scaling factor. (cf. the second line in (50).) The reader is referred to [1] to see the agreement between the homogeneous Green's function and the modified implementation of the k-Wave. To see the agreements in a smoothly varying heterogeneous medium, the reader is referred to [1] and figures 3(a) and 3(b) in this manuscript.

## REFERENCES

- [1] A. Javaherian and B. Cox, Ray-based inversion accounting for scattering for biomedical ultrasound tomography, *Inverse Problems* vol. 37, no.11, 115003, 2021.
- [2] N. Duric P. Littrup, L. Poulo, A. Babkin, R. Pevzner, E. Holsapple, O. Rama and C. Glide, Detection of breast cancer with ultrasound tomography: First results with the Computed Ultrasound Risk Evaluation (CURE) prototype, *Med. Phys.* vol. 34, no.2, 2007.
- [3] T. Hopp, N. Ruiter, J. C. Bamber, N. Duric and K.W.A. van Dongen (Eds.) 2017 International Workshop on Medical Ultrasound Tomography, Speyer, Germany.
- [4] P. Koulountzios, T. Rymarczyk and M. Soleimani, A Triple-Modality Ultrasound Computed Tomography Based on Full-Waveform Data for Industrial Processes, in *IEEE Sensors Journal*, vol. 21, no. 18, pp. 20896-20909, 2021, doi: 10.1109/JSEN.2021.3100391.
- [5] P. Koulountzios, T. Rymarczyk and M. Soleimani, A 4-D Ultrasound Tomography for Industrial Process Reactors Investigation, in *IEEE Trans Instrum Meas*, vol. 71, pp. 1-14, 2022, Art no. 4502714, doi: 10.1109/TIM.2022.3164166.
- [6] C. Li, N. Duric, P. Littrup and L. Huang, In-vivo breast sound speed imaging with ultrasound computed tomography, *Ultrasound in Med. & Biol.*, vol. 35, no. 10, pp. 1615–1628, 2009.
- [7] N. V. Ruiter, M. Zapf, T. Hopp, R. Dapp, E. Kretzek, M. Birk, B. Kohout, H Gemmeke, 3D ultrasound computer tomography of the breast: A new era?, *European Journal of Radiology*, vol. 81, Supplement 1, pp. S133-S134, 2012.
- [8] H. Gemmeke, T. Hopp, M. Zapf, C. Kaiser, N.V. Ruiter, 3D Ultrasound Computer Tomography: Hardware Setup, Reconstruction Methods and First Clinical Results, *NUCL INSTRUM METH A*, vol. 873, 2017, pp. 59-65, 2017.

- [9] K. J. Opielinski, P. Pruchnicki, P. Szymanowski, W. K. Szepieniec, H. Szweda, E. Swis, M. Jozwik, M. Tenderenda and M. Bulkowskif, Multimodal ultrasound computer-assisted tomography: An approach to the recognition of breast lesions, *COMPUT MED IMAG GRAP* vol. 65, pp. 102–114, 2018.
- [10] C. Li, L. Huang, N. Duric, H. Zhang, and C. Rowe, An improved automatic time-of-flight picker for medical ultrasound tomography, *Ultrasonics*, vol. 49, pp. 61-72, 2009.
- [11] R. Gerhard Pratt, C. Shin and G. J. Hicks, Gauss-Newton and full Newton methods in frequency-space seismic waveform inversion, *Geophys. J. Int.*, vol. 133, pp. 341-362, 1998.
- [12] R.-E. Plessix, A review of the adjoint-state method for computing the gradient of a functional with geophysical applications, *Geophys. J. Int.* vol. 167, pp. 495–503, 2006.
- [13] J. Wiskin, D. T. Borup, S. A. Johnson and M. Berggren, Non-linear inverse scattering: high resolution quantitative breast tissue tomography, *J. Acoust. Soc. Am.*, vol. 131, no. 5, pp. 3802-13, 2012.
- [14] K. Wang, T. Matthews, F. Anis, C. Li, N. Duric, and M. A. Anastasio, Waveform inversion with source encoding for breast sound speed reconstruction in ultrasound Computed Tomography, *IEEE T ULTRASON FERR*, vol. 62, no. 3, 2015.
- [15] J. W. Wiskin, D. T. Borup, E. Iuanow, J. Klock, M. W. Lenox, 3-D Nonlinear Acoustic Inverse Scattering: Algorithm and Quantitative Results, *IEEE T ULTRASON FERR*, vol. 64, no. 3, 2017.
- [16] A. V. Goncharsky and S. Y. Romanov, Iterative methods for solving coefficient inverse problems of wave tomography in models with attenuation, *Inverse Problems*, vol. 33, pp. 025003, 2017.
- [17] T. P. Matthews, K. Wang, C. Li, N. Duric, and M. A. Anastasio, Regularized Dual Averaging Image Reconstruction for Full-Wave Ultrasound Computed Tomography, *IEEE T ULTRASON FERR*, vol. 64, no. 5, 2017.
- [18] T. P. Matthews and M. A. Anastasio, Joint reconstruction of the initial pressure and speed of sound distributions from combined photoacoustic and ultrasound tomography measurements, *Inverse Problems*, vol. 33, pp. 124002, 2017.
- [19] M. Pérez-Liva, J. L. Herraiz, J. M. Udias, E. Miller, B. T. Cox, and B. E. Treeby, Time domain reconstruction of sound speed and attenuation in ultrasound computed tomography using full wave inversion, *J. Acoust. Soc. Am.*, vol. 141, no. 3, pp. 1595-1604 2017. doi: 10.1121/1.4976688.
- [20] L. Guasch, O. Calderón Agudo, M. Tang, P. Nachev, and M. Warner, Full-waveform inversion imaging of the human brain. *Nature Digital Medicine*, vol. 3, 28, 2020.
- [21] A. J. Devaney, Inverse-scattering theory within the Rytov approximation, *Opt. Lett.* vol. 6, no. 8, pp. 374-376, 1981.
- [22] A. J. Devaney, A filtered backpropagation algorithm for diffraction tomography, *Ultrason. Imag.*, vol. 4, pp. 336–350, 1982.
- [23] A. J. Devaney and M. L. Oristaglio, Inversion procedure for inverse scattering within the distorted-wave Born approximation, *Physical Review Letters*, vol. (51), no. 4, 1983.
- [24] W. B. Beydoun and A. Tarantola, First Born and Rytov approximations: Modelling and inversion conditions in a canonical example, *J. Acoust. Soc. Am.*, vol. 83, pp. 1045-1055, 1988.
- [25] D. T. Borup, S. A. Johnson, W. W. Kimz and M. J. Berggren, Nonperturbative Diffraction tomography via Gauss-Newton iteration applied to the scattering integral equation, *Ultrasonic Imaging*, vol. 14, pp. 69-85, 1992.
- [26] T.D. Mast, Aberration correction for time-domain ultrasound diffraction tomography, *J. Acoust. Soc. Am.*, vol. 112, no. 1, 2002.
- [27] F. Simonetti, L. Huang, N. Duric, and P. Littrup, Diffraction and coherence in breast ultrasound tomography: A study with a toroidal array, *Med. Phys.*, vol. 36, pp. 2955, 2009.
- [28] P. Mojabi and J. Lovetri, Ultrasound tomography for simultaneous reconstruction of acoustic density, attenuation, and compressibility profiles, *J. Acoust. Soc. Am.* vol. 137, no. 4, 2015.
- [29] X. Yun, J. He, A. Carevic, I. Slapnicar, J. Barlow and M. Almekkawy, Reconstruction of ultrasound tomography for cancer detection using total least squares and conjugate gradient method, Proc. SPIE 10580, Medical Imaging 2018: Ultrasonic Imaging and Tomography, 105800K (6 March 2018); doi: 10.1117/12.2293906.
- [30] Carevic, X. Yun, G. Lee, I. Slapnicar, A. Abdou, J. Barlow and M. Almekkawy, Solving the ultrasound inverse scattering problem of inhomogeneous media using different approaches of total least squares algorithms, Proc. SPIE 10580, Medical Imaging 2018: Ultrasonic Imaging and Tomography, 105800J (6 March 2018); doi: 10.1117/12.2293627.
- [31] Carevic, X. Yun and M. Almekkawy, Adaptive truncated total least square on distorted born iterative method in ultrasound inverse scattering problem, Proc. SPIE 10955, Medical Imaging 2019: Ultrasonic Imaging and Tomography, 1095515 (15 March 2019); doi: 10.1117/12.2512416.

- [32] P. Huthwaite and F. Simonetti, High-resolution imaging without iteration: a fast and robust method for breast ultrasound tomography, *J. Acoust. Soc. Am.*, vol. 130, no. 3, pp. 1721-34, 2011.
- [33] P. Thierry, S. Operto, and G. Lambare, Fast 2-D ray+Born migration/inversion in complex media, *GEO-PHYSICS*, Vol. 64, No. 1, pp. 162–181, 1999.
- [34] V. Červený, Seismic ray theory, Cambridge University Press. 2001.
- [35] S. Jin, R. Madariaga, J. Virieux, and G. Lambaré, Two-dimensional asymptotic iterative elastic inversion, *Geophys. J. Internat.*, Vol. 108, No.2, pp. 575–588, 1992.
- [36] G. Lambare, J. Virieux, R. Madariaga, and S. Jin, Iterative asymptotic inversion in the acoustic approximation, *GEOPHYSICS*, Vol. 57. No. 9, pp. 1138-1154, 1992.
- [37] G. Lambare, S. Operto, P. Podvin, and P. Thierry, 3D ray+Born migration/inversion—Part 1: Theory, *GEO-PHYSICS*, Vol. 68, No. 4, 2003.
- [38] H. S. Aghamiry, A. Gholami, S. Operto, Complex-Valued Imaging with Total Variation Regularization: An Application to Full-Waveform Inversion in Visco-acoustic Media, *SIAM J. IMAGING SCIENCES*, Vol. 14, no. 1, pp. 58-91, 2021.
- [39] [www.k-Wave.org](http://www.k-Wave.org)
- [40] B. E. Treeby and B. T. Cox, k-Wave: MATLAB toolbox for the simulation and reconstruction of photoacoustic wave fields *J. Biomed. Opt.* vol. 15, no. 2, 021314, 2010.
- [41] A. Javaherian, F. Lucka and B. Cox, Refraction-corrected ray-based inversion for three-dimensional ultrasound tomography of the breast, *Inverse Problems*, vol. 36, 125010, 2020.
- [42] J. F. Kelly, R. J. McGough, and M. M. Meerschaert, Analytical time-domain Green’s functions for power-law media, *J. Acoust. Soc. Am.*, vol. 124, no. 5, pp. 2861–2872, 2008.
- [43] T. L. Szabo, Time domain wave equations for lossy media obeying a frequency power law, *J. Acoust. Soc. Am.*, vol. 96, pp. 491–500, 1994.
- [44] M. Liebler, S. Ginter, T. Dreyer, and R. E. Riedlinger, “Full wave modeling of therapeutic ultrasound: Efficient time-domain implementation of the frequency power-law attenuation, *J. Acoust. Soc. Am.*, vol. 116, pp. 2742–2750, 2004.
- [45] B. Petrovic and S. Parolai, Joint Deconvolution of building and downhole strong-motion recordings: evidence for the seismic wavefield being radiated back into the shallow geological layers, *Bulletin of the Seismological Society of America*, Vol. 106, no. 4, pp. 1720–1732, August 2016.
- [46] Pierce A D 1981 Acoustics: An Introduction to its Physical Principles and Applications 3rd Edition (Berlin: Springer and ASA Press) (<https://doi.org/10.1007/978-3-030-11214-1>)
- [47] J.C. Butcher, The numerical analysis of ordinary differential equations. Runge–Kutta and general linear methods, Wiley, 1987.
- [48] E. Kreyszig, 1993 Advanced engineering mathematics. John Wiley & Sons, Inc., New York.
- [49] J. Virieux and V. Ferra Ray tracing in 3D complex isotropic media: An analysis of the problem, *GEOPHYSICS*, vol. 56, no. 12, pp. 2057-2069, 1991.
- [50] A. H. Anderson and A. C. Kak, Digital ray tracing in two-dimensional refractive fields, *J. Acoust. Soc. Am.*, vol. 72, pp. 1593-1606, 1982.
- [51] V. červený, T. J. Moser, Ray propagator matrices in three-dimensional anisotropic inhomogeneous layered media, *Geophys. J. Int.* Vol. 168, pp. 593–604, 2007.
- [52] Y. Lou, W. Zhou, T. P. Matthews, C. M. Appleton and M. A. Anastasio, Generation of anatomically realistic numerical phantoms for photoacoustic and ultrasonic breast imaging, *J Biomed Opt.*, vol. 22, no. 4, pp. 041015, 2017.
- [53] E. S. Wise, B. T. Cox, J. Jaros, B. E. Treeby, Representing arbitrary acoustic source and sensor distributions in Fourier collocation methods, *J. Acoust. Soc. of Am.*, vol. 146, no. 1, pp. 278-288, 2019.
- [54] M. Tabei, T. D. Mast, and R. C. Waag, “A k-space method for coupled first-order acoustic propagation equations,” *J. Acoust. Soc. Am.* vol. 111, pp. 53–63, 2002.
- [55] B. Petrovic and S. Parolai, Joint Convulsion of Building and Downhole strong-motion recordings: evidence for the seismic wavefield being radiated back into the shallow geological layers, *Bulletin of the Seismological Society of America*, Vol. 106, No. 4, pp. 1720–1732, 2016, doi: 10.1785/0120150326.
- [56] A. H. Anderson and A.C. Kak, Simultaneous algebraic reconstruction techniques (SART): A superior implementation of the ART algorithm, *Ultrasonic Imaging*, vol. 6, no. 1, pp. 81-94, 1984.
- [57] K-Wave, A Matlab toolbox for the time domain simulation of acoustic wave fields, user manual,